# Cyber-Physical Dynamic System (CPDS) Modeling for Frequency Regulation and AGC Services of Distributed Energy Resources

Wenbo Wang,[1] Xin Fang,[1] Hantao Cui,[2,3] Jinning Wang,[2] Fangxing Li,[2] Yijing Liu,[4] Thomas J. Overbye,[4] Mengmeng Cai,[1] and Chris Irwin[5]

1 National Renewable Energy Laboratory
2 University of Tennessee
3 Oklahoma State University
4 Texas A&M University
5 U.S. Department of Energy

# Cyber-Physical Dynamic System (CPDS) Modeling for Frequency Regulation and AGC Services of Distributed Energy Resources

Wenbo Wang,[1] Xin Fang,[1] Hantao Cui,[2,3] Jinning Wang,[2] Fangxing Li,[2] Yijing Liu,[4] Thomas J. Overbye,[4] Mengmeng Cai,[1] and Chris Irwin[5]

1 National Renewable Energy Laboratory
2 University of Tennessee
3 Oklahoma State University
4 Texas A&M University
5 U.S. Department of Energy

**NOTICE**

# Foreword

This project began in October 2020 and has a total duration of 1.5 years. It was conducted primarily at the National Renewable Energy Laboratory, in collaboration with the University of Tennessee at Knoxville.

# Preface

This project aims to develop an open-source, scalable, transmission, distribution, and communication, dynamic co-simulation framework to study the impacts of communication failures of distributed energy resources (DERs) providing frequency regulation services on electric power system stability. The project will significantly contribute to the reliability and security of modeling DER integration in future transmission-and-distribution (T&D) networks. In addition, we collaborated with university partners to test and validate the methodology, considering primary frequency response and secondary frequency response together, by integrating the proposed framework into the simulated T&D networks of a large interconnected system: a synthetic Texas 2,000-bus transmission network combined with more than 1 million distribution buses.

# Acknowledgments

# List of Acronyms

| | |
|---|---|
| ACE | area control error |
| AGC | automatic generation control |
| CDPD | Cellular Digital Packet Data |
| CPDS | cyber-physical dynamic system |
| DER | distributed energy resource |
| DPV | distributed photovoltaic |
| EMT | electromagnetic transient |
| EPRI | Electric Power Research Institute |
| EV | electric vehicle |
| FESTIV | Flexible Energy Scheduling Tool for Integrating Variable Generation |
| HELICS | Hierarchical Engine for Large-Scale Infrastructure Co-Simulation |
| HPC | high-performance computer |
| IEEE | Institute of Electrical and Electronics Engineers |
| LFC | load frequency control |
| MPPT | maximum power point tracking |
| NREL | National Renewable Energy Laboratory |
| PEV | plug-in electric vehicle |
| PFR | primary frequency response |
| PI | proportional integral |
| PV | photovoltaic |
| QSTS | quasi-static time series |
| SFR | secondary frequency response |
| SMUD | Sacramento Municipal Utility District |
| SOC | state of charge |
| T&D | transmission-and-distribution |
| TPDA | Three Phase Dynamics Analyzer |
| V2G | vehicle-to-grid |
| VSM | voltage-power sensitivity matrix |

# Executive Summary

Distributed energy resources (DERs) are being rapidly deployed in distribution networks, which brings new challenges and opportunities to balancing the power system and stabilizing the system frequency. For reliable power system operation, regulation services are used to stabilize the system frequency through automatically balancing the system generation and load. This means that in the future, high- penetration, renewable power system, additional and alternative reliable frequency regulation service providers, such as distributed energy storage resources, should be explored.

Although the capability of utility-scale energy storage to provide frequency regulation services has been demonstrated, the integrated control and dynamic modeling of DERs providing frequency regulation grid services has been rarely explored. There are several challenges to adopting DERs to provide reliable grid services, as illustrated in Federal Energy Regulatory Commission Order 755 [1]. First, the distributed installation of distributed energy storage requires comprehensive cyber-physical dynamic system (CPDS) modeling to fully consider the impacts of the communication latency variability on the real-time frequency regulation provision capability of DERs, as shown in Figure ES-1. Unlike conventional generators, there are typically two-layer communications between DERs and system operators, which increases the communication delay. Also, unlike conventional generators, whose dynamics have been comprehensively studied and modeled, modeling the power-dynamic characteristics of individual DERs (Figure ES-1) is challenging when considering accurate representation of automatic generation control (AGC) and their power-frequency relationships. Third, the temporal dependent state-of-charge uncertainty of DERs creates challenges for look-ahead generation scheduling when considering their power and frequency regulation capacities; therefore, the aggregator should optimize the frequency regulation provision from individual DERs in real time.
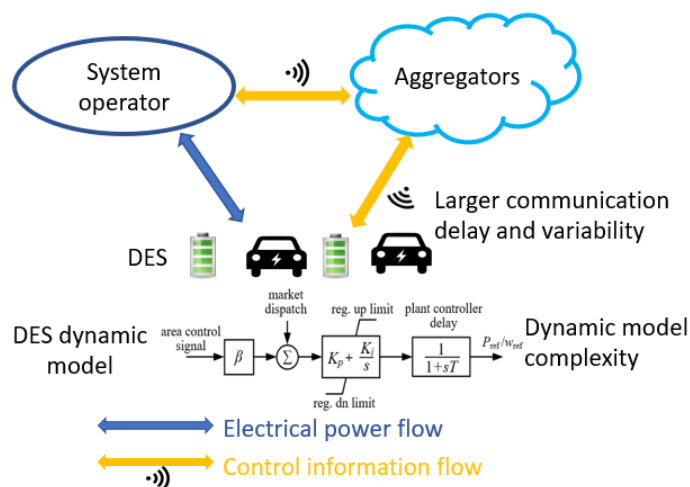


**Figure ES-1. Illustration of the DER CPDS model for the provision of reliable frequency regulation services**

To overcome these challenges, this project proposes a CPDS model to capture the uncertainty of the two-layer communication latency and power dynamics of DERs. The variability of the DER communication delays and dynamic constraints are comprehensively modeled in this work (as

shown in Figure ES-1). The DER AGC model with communication delay is designed to validate distributed energy storage's frequency regulation services. Like current performance-based frequency regulation evaluation, the delivery of the DER frequency regulation will be assessed through post-analysis of the actual AGC response with respect to the AGC control signal from system operators. Consequently, the reliability improvement with DERs providing reliable frequency regulation services can be evaluated from a comprehensive perspective considering all the dynamics of communications and power.

Key findings from this project include:

- The need for co-simulation, different from the traditional analytical method (i.e., state-space equations), co-simulation method can observe different aspects of the impacts, e.g., heterogeneous communication impacts and local grid constraints, such as voltage and reverse power flow. The quantitative analysis and modeling scheme in this report can provide insights into designing future load frequency control (LFC) algorithms and communication planning for LFC with DERs such as distributed photovoltaics (DPVs) and plug-in electric vehicles (PEVs).

- The communication delay margin of DER AGC can be quite different from that of conventional generators, risk of system instability might substantially increase if the design of the DER AGC control fails to consider communication variations; Therefore, system operators should consider communication delays when designing DER AGC control parameters and when dispatching DERs for AGC services. One example is demonstrated in Figure ES-2, where it shows different communication delay times affect the system frequency after contingencies.

- The aggregation of PEVs has great potential to provide both primary frequency regulation (PFR) and secondary frequency regulation (SFR) to quickly restore the system frequency after contingencies. Several factors can impact PEV frequency regulation, such as the participation factor and the potential state of charge (SOC) limits.

- PEV frequency regulation with communication variations demonstrate that the mean values of the communication delay have a higher impact on the frequency recovery than the standard deviation of the delay. Meanwhile, the packet drop impacts on the frequency restoration are not significant in both the homogeneous and heterogeneous packet drop rates, this is demonstrated in Figure ES-3, more details can be found in chapter 6.
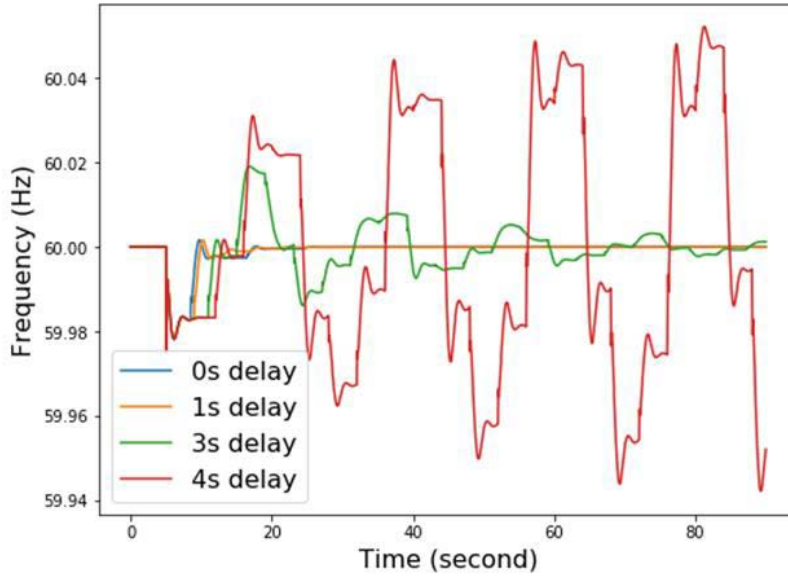
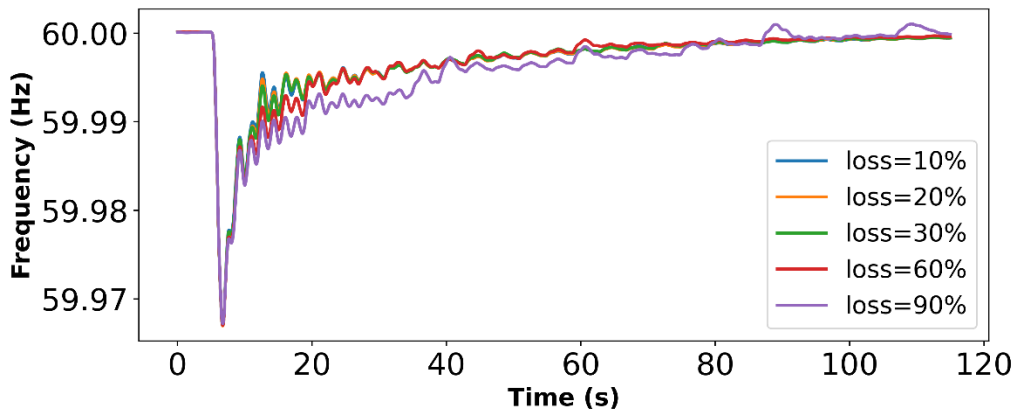**Figure ES-2. System frequency response under different delays**



**Figure ES-3. Homogeneous packet loss with different loss rates**

# Table of Contents

# List of Figures

# List of Tables

# 1  Introduction

Distributed energy resources (DERs) are being rapidly deployed in distribution networks, which brings new challenges to balancing the power system and stabilizing the system frequency [2]. The power output of DERs, if not optimally managed, can not only impact the local distribution voltage but also deteriorate the transmission system power balance and increase frequency fluctuations [3], [4], [5]. Frequency regulation services—including primary frequency response (PFR), secondary frequency response (SFR), and tertiary frequency response—are used to maintain real-time power system balance and frequency stability. DERs, equipped with advanced control strategies, have the capability to provide these services [6]–[9]. The recent Federal Energy Regulatory Commission Order 2222 [10] stipulates that electricity markets should remove all market access barriers to DERs to allow them to participate in the energy, capacity, and ancillary services markets; therefore, to better understand and use DER frequency regulation services, the frequency dynamic responses of DERs should be modeled in dynamic system simulations, and efficiently integrating DER dynamics into dynamic transmission system frequency simulations has been attracting increasing research attention. The power output of DERs, which are hosted mainly in distribution networks, impacts the local distribution voltage profile, especially when their penetration level is high; therefore, when using DERs to provide frequency regulation services, the local voltage profile should be optimized to avoid over-/undervoltage issues in the distribution network.

Existing dynamic simulation tools—such as GE PSLF, PowerWorld Simulator, and Siemens PTI PSS/E [11]–[13]—have been developed mainly for transmission frequency dynamic analysis, where the positive-sequence model is used with the balanced, three-phase assumption; therefore, to study the impacts of DER dynamics, an aggregated model is usually used, such as DER_A [14]. Distribution networks hosting DERs, however, are normally three-phase, unbalanced, and the DER power outputs for the frequency response should not violate the local voltage constraints. There exists research focusing on the steady-state or quasi-static analysis of transmission-and-distribution (T&D) networks with DERs. For instance, the authors of [15] proposed an interfacing variables updating algorithm between the transmission and distribution systems to improve the convergence of the T&D steady-state power flow co-simulation. The accuracy and computational efficiency of three T&D coupling protocols (decoupled, loosely coupled, and tightly coupled) was evaluated in [16] for quasi-static T&D co-simulation. The coupled T&D AC optimal power flow in [17] used a coordinated T&D structure with a heterogeneous decomposition algorithm. The simulation tools, synchronization methods, and potential research topics about T&D co-simulation were reviewed in [18]. In [19], the impacts of DERs on the economic operation of the transmission system were investigated in an integrated grid modeling system.

For T&D dynamic analysis with DERs, electromagnetic transient (EMT) simulation tools can simulate both T&D network dynamics; however, the full EMT simulation for T&D networks requires extensive simulation time—even for a medium-size network [20]. The authors of [21], [22] proposed modeling and simulating power system electromechanical transients and EMTs by a very large-scale integrated circuit to improve simulation efficiency. Using the full EMT simulation to simulate large-scale T&D networks is considered computationally impractical. In [23], a hybrid EMT and phasor-domain simulation model was proposed to accelerate the EMT

1

simulation for T&D networks. The EMT simulation was accelerated by switching between the detailed EMT simulation and the phasor-domain simulation. In [24], an integrated T&D system power flow and dynamic simulation (transient stability dynamics) was proposed, where the T&D systems are represented in three sequences and three phases in detail, respectively. The TPDA in [25] solved differential algebraic equations for the unbalanced electromechanical transients using the Park transformation. Reference [26] built a three-phase, unbalanced transient dynamic (electromechanical transient) and power flow model for distribution systems/microgrids with synchronous generators. Reference [27] focused on distribution systems and proposed a hybrid simulation tool to study the impacts of distributed photovoltaics (DPV) in distribution networks. DPV was modeled with EMT models to study their fast dynamics, interfacing feeder models in OpenDSS in [28]. Reference [29] built a generic platform for T&D dynamic co-simulation in the framework for network co-simulation, where dynamic simulations were used for both T&D systems. In [30], T&D dynamic co-simulation models with parallel and series computation schemes were compared, along with a discussion on the integration time step impacts. Reference [31] used a coupled T&D simulation to analyze the impacts of bulk power system faults on the distribution generation response. A comparison of different T&D co-simulation models, their transmission/distribution simulators, and the tested transmission/distribution networks is shown in Table 1.

**Table 1. Comparison of Different T&D Co-Simulation Models**

| Reference | Model | Trans. Simulator | Dist. Simulator | Trans. Network | Dist. Network |
|---|---|---|---|---|---|
| [15], [16] | Static | MATLAB | OpenDSS | IEEE[a] 9-bus system/ IEEE 39-bus system | EPRI[b] Ckt-24 |
| [17] | Static | MATLAB | MATLAB | IEEE 14-bus system | IEEE 57-bus system |
| [19] | Static | FESTIV[c]/ MATPOWER | GridLAB-D | SMUD[d] 250-bus system | SMUD distribution feeders |
| [23] | Dynamic | Integrated in PSCAD/EMTDC/InterPSS | | IEEE 9-bus system | 4-bus sub-trans. and dist. |
| [24] | Dynamic | Three-sequence model | Three-phase model | IEEE 9-bus system/ IEEE 39-bus system | 8-bus distribution feeder |
| [25] | Dynamic | Integrated in TPDA[e] | | IEEE 39-bus systems | Utility model |
| [26] | Dynamic | No trans. | GridLAB-D | No trans. | IEEE 123-node distribution test feeder |
| [27] | Dynamic | No trans. | EMT/ OpenDSS | No trans. | IEEE 8,500 node |
| [29] | Dynamic | Dynamic three-phase model | GridLAB-D | IEEE 9-bus system | IEEE 13-node distribution feeder |
| [30] | Dynamic | PSAT | OpenDSS | IEEE 39-bus system | 5,780-node distribution system |
| [31] | Dynamic | PSLF | OpenDSS | WECC | Three California feeders |
| This work | Dynamic | ANDES | OpenDSS | ACTIVSg2000 | More than 1 million-node distribution networks |

[a] Institute of Electrical and Electronics Engineers
[b] Electric Power Research Institute
[c] Flexible Energy Scheduling Tool for Integrating Variable Generation
[d] Sacramento Municipal Utility District
[e] Three Phase Dynamics Analyzer

3

Unlike conventional generators, which use a dedicated communication channel to provide automatic generation control (AGC) [32], DERs can use open communication networks to exchange control signals with system control centers, possibly through DER aggregators [33]. The open networks expose several vulnerabilities of the DER AGC services, such as extended communication latency, increased packet loss, and cyberattacks (e.g., false data injection); therefore, it is imperative to study the impact of the communication variations in DER AGC on the system frequency stability to ensure reliable operation of the future electric grid with high penetrations of DERs. Although it depends on the specific communication infrastructure, normal time delays—ranging from several tens to hundreds of milliseconds—are introduced in transmitting and processing remote signals [34], [35]. These delays will likely increase when open communication networks (e.g., mobile or fixed broadband) and multilayer structures (DER aggregators) are introduced, especially during periods of congested communication because of the large amount of data exchanged.

Overall, there is a lack of T&D dynamic co-simulation research while considering communication impacts that focuses on DER frequency regulation, including both PFR and SFR, in large-scale systems. For instance, DERs provide frequency regulation by adjusting their active power outputs, but DERs might be required by local distribution operators to adjust power to maintain certain voltage ranges, and the overall dynamic interactions between T&D networks are still unknown. To account for DER frequency regulation responses in T&D networks, this project develops an efficient, open-source, T&D frequency dynamic co-simulation framework, namely Cyber-Physical Dynamic System (CPDS), wherein the well-established T&D simulation tools are leveraged: the high-performance transmission dynamic simulation tool ANDES [36] and the distribution network solver OpenDSS [28]. The co-simulation platform is built with the Hierarchical Engine for Large-Scale Infrastructure Co-Simulation (HELICS) [37]–[39] to establish the co-simulation flow between the transmission dynamic simulations and the distribution quasi-static time-series (QSTS) power flow simulations. To synchronize the DER frequency response hosted by distribution networks with the transmission network, DERs are modeled with detailed frequency dynamics. The DER power outputs from the time domain simulation are exchanged with the distribution power flow simulators through HELICS. Consequently, the DER frequency dynamic responses are considered in both the transmission frequency dynamic simulation and the distribution network power flow simulation with multiple time resolutions. Built on this architecture, along with the efficient subsystem simulators, the proposed T&D frequency dynamic co-simulation framework is computationally efficient. As shown in Table 1, the proposed framework is the first-of-its-kind T&D dynamic co-simulation model that can perform dynamic simulations with a 2,000-bus transmission network, ACTIVSg2000 [40], and distribution networks with more than 1 million nodes. In summary, this work has the following contributions:

- An open-source, T&D frequency dynamic co-simulation framework is developed to study DER PFR and SFR in large-scale T&D networks. In this framework, we propose a novel implementation to synchronize the transmission dynamic simulation and the distribution QSTS simulation for DER PFR and SFR. The DER power intermittency and local distribution voltage constraints are also considered in the PFR and SFR provision. This real-time maximum power modeling of DERs considers both the availability uncertainty and the local voltage constraints.

- The efficiency and scalability of the T&D dynamic co-simulation framework is further demonstrated with a generation trip scenario in an integrated T&D system with a 2,000-bus transmission network and distribution networks with more than 1 million distribution nodes.
- A few practical use cases are considered here, which demonstrate the capabilities and potential applications of the framework.

The rest of this report is organized as follows: Section 2 presents the overall T&D frequency dynamic co-simulation framework using HELICS [41]. Section 3 introduces the T&D network frequency dynamic model with DERs [41]. Section 4 performs the case study to demonstrate the DER PFR and SFR [41]. Section 5 shows the communication delay margin of DERs providing SFR [42]. Section 6 performs the simulation with electric vehicles (EVs) providing PFR and SFR with a communication delay [43]. Section 7 concludes the paper.

5

# 2 Transmission-Distribution-Communication Dynamic Co-simulation Framework

The T&D&C dynamic co-simulation framework developed for DER frequency dynamic response is based on the HELICS platform and off-the-shelf power system simulators. This section introduces the components of the framework and develops the interfacing requirements.

## 2.1 Brief Description of HELICS

HELICS is an open-source, cyber-physical co-simulation framework for energy systems. It is designed to integrate simulators of transmission, distribution, and communication domains to simulate regional and interconnection-scale power system behaviors. Because it exploits a generalized data exchange interface, it can include other energy sectors' simulator as well. A few key concepts of HELICS that are relevant here are introduced in the following; for more details, see [37], [38]:

- Federates run simulation instances of individual subsystems, sending and receiving physical and control signals to and from other federates.
- Brokers maintain synchronization in the federation (i.e., many federates) and facilitate message exchanges among federates.
- Simulators are executable—that is, they can perform some analysis functions. In this context, for example, they are the transmission simulator ANDES and the distribution simulator OpenDSS. Note that the terms *federate* and *simulator* are used interchangeably in this paper.
- Messages are the information passed between federates during the execution of the co-simulation. The message exchange is realized through either defining subscription and publication functions or by dedicated federate-to-federate end point communications. Note that the filter defining the communication delay or packet drops can be included in the end point communications to simulate the cyber-physical interactions in the co-simulation.

## 2.2 T&D&C Co-Simulation Information Exchange and Interface

The T&D simulators can execute with individual federates (e.g., separate configuration files in Python or even on multiple machines with different operating systems in various languages), the time synchronization is maintained by a HELICS broker, and then the information exchange needs to be defined next.

Assume the power system comprises transmission and distribution systems; local turbine governors that control the frequency dynamic response of the turbine governors of conventional generators; and DER aggregators that control the individual DER's frequency response. In the co-simulation framework, the information exchange among simulators in terms of simulation time is configured as loosely coupled (i.e., one inter-time step variable exchange between simulators without intra-time step iterations), as shown in Figure 1. The information exchanges take place in series such that the co-simulation is robust; the impacts of the series or parallel in the information exchange can be found in [30]. For demonstration, only one transmission network and one distribution network are shown in Figure 1.

The distribution system unbalanced, three-phase power injection/withdraw (at the substation) are converted into the positive-sequence power injection/withdraw using the formulation (1)–(3) To match the per-unit positive-sequence equivalent calculation in the transmission simulator, [44]:

$$S_i^+ = TS_i^{abc} \tag{1}$$
$$S_i^+ = P_i^+ + jQ_i^+ \tag{2}$$
$$T = [1/3 \quad 1/3 \quad 1/3] \tag{3}$$

where $S_i^+$ is the power at bus i in the transmission positive-sequence dynamic model, and $S_i^{abc}$ is the three-phase power of the distribution network connecting the transmission bus i.

Note that the HELICS platform can coordinate multiple simulations of independent distribution networks connected to the transmission network in parallel. The time steps of the T&D simulators can be different. Their information exchange is synchronized by HELICS. The dashed arrow pointing to the right denotes the simulation time; the dashed rectangles denote the changing states (in terms of simulation time) of the T&D simulators. This is also true when both the conventional generation turbine governor simulators and the DER aggregator simulators are added.
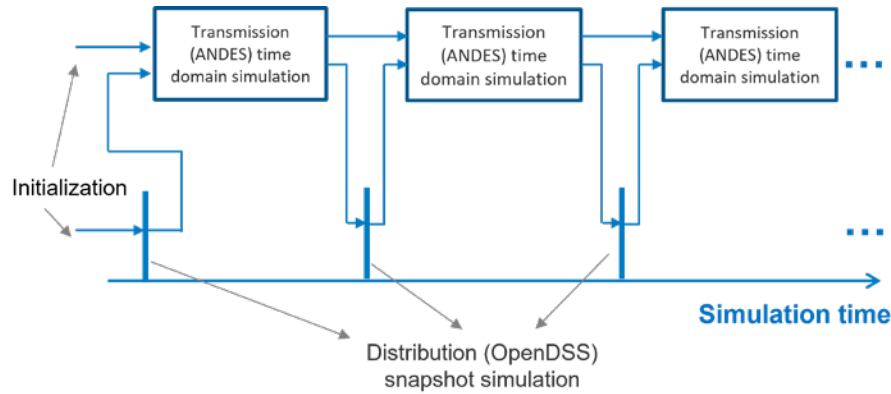


**Figure 1. Simulation time flow demonstration, note that because the distribution snapshot simulation with time duration virtually 0, it is represented as vertical line (rectangle with width 0).**

The detailed information exchanged among simulators is shown in Figure 2Figure 2Figure 2. The arrows denote the information exchange directions, with the exchange step time displayed, which can be changed based on the simulation settings. The blue boxes and arrows represent the physical power system simulators and variables, whereas the orange boxes and arrows represent the communication simulators and control signals. The transmission simulator and the distribution simulator exchange the physical variables every second, including active power and voltage magnitude at the feeder heads, through subscription/publication in HELICS. The power of the DERs is also exchanged to ensure their consistent output in both the transmission and distribution systems. The transmission internal simulation time step is two cycles (33.3 milliseconds) under normal conditions. This internal step time will be adaptively reduced during the transient to improve convergence. The transmission dynamic simulator sends the system frequency and the area control error (ACE) signals to the transmission control center through end points in HELICS. The control center calculates the AGC signal and sends it the conventional generation turbine governor and the DER aggregator every 4 seconds through end points. The

7

turbine governors and aggregators execute their AGC through changing the power set points in their dynamic generation model in the transmission dynamic simulator every 0.5 second. This AGC time step can be changed based on the system settings.
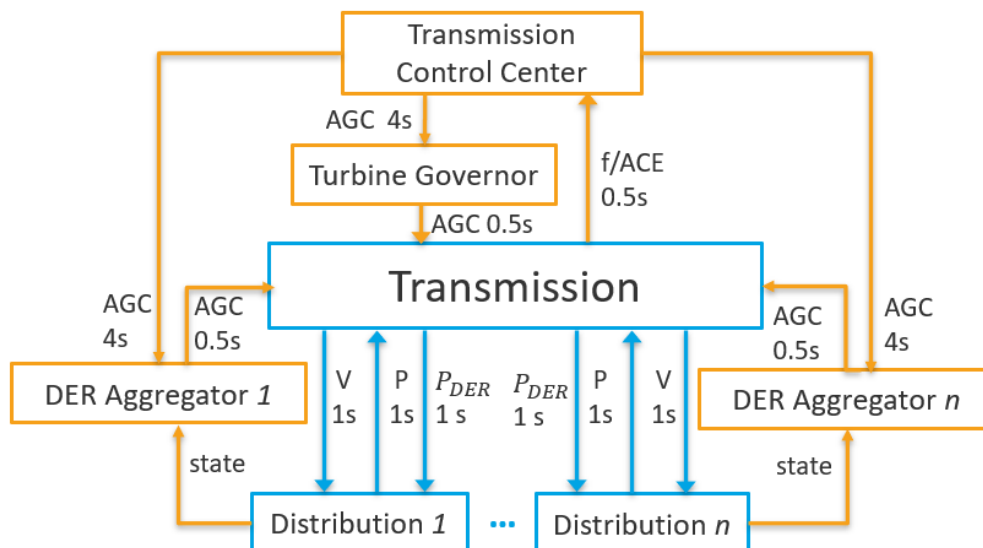


**Figure 2. Information exchange and time steps**

Reference [15] discussed the iterative coupling of the exchange variables between the transmission and distribution simulators. The co-simulation model in [15] was a steady-state power flow co-simulation model, the iteration between the T&D systems was for the same snapshot, and the interfacing variables iterate between T&D at every time step until convergence. In the proposed T&D dynamic co-simulation, however, the transmission simulator is performing the time domain simulation for the electromechanical dynamic analysis; therefore, it is not practical to iterate the interfacing variables between the T&D systems at every time step. The reasons are described as follows: to enable this iterative coupling in the dynamic co-simulation, the transmission system dynamic simulation needs to store all intermediate state variables in the time domain simulation, which is not possible in the commercial dynamic simulation tools (such as PSSE, PowerWorld Simulator, and PSLF) or the open-source ANDES because none of these tools save intermediate state variables to speed up the dynamic simulation. Note that the study in [15] demonstrates that when the time step of the co-simulation is small, the accuracy of the loose coupling increases. In the proposed dynamic co-simulation, the time step between the T&D systems is very small (1 second or 0.5 second); therefore, the current noniterative coupling between T&D can obtain highly accurate results.

## 2.3 Communication Considerations: Designated Channels Versus Open Networks

Conventional load frequency control (LFC) is transmitted through designated private communication channels. It is relatively reliable, and the time delay normally ranges from 80–200 milliseconds [45]; however, to enable grid services from EVs, aggregators of numerous EVs might send power dispatch commands wirelessly to the vehicle, and therefore the wireless open communication networks are likely used instead of a designated private communication network. This method also avoids the high cost of connecting a large number of EVs using private

8

channels. The smart charging demonstration project in [46] used Cellular Digital Packet Data (CDPD, i.e., 2G family) to communicate between the aggregator and EVs. The project also showed that there was a latency of 400–2,000 milliseconds among all packets being transmitted; note that these values include battery response time. A different test in [47] did not use wireless communications but leveraged the communication link inside the connector (the charging cable of EVs) and thus required plugging in; then, with the help of a specially designed board mounted on the vehicle and based on the SAE J1772 standard, this formed a communication connection between the charging station and the vehicle. Under the assumption that charging stations or buildings can be aggregators, the authors in [48] discussed different wireless communication techniques to be considered between the aggregator and individual EVs: Zigbee, near-field communication, Bluetooth, IEEE 802.11p, and WiMAX; however, these technologies cover a limited distance, from 10 m–5 km. It is promising that cellular network technologies (i.e., 4G, 5G used by mobile phone devices) and cloud services can fulfill the needs of smart charging— they are fast, mobile, inclusive, and easy to access, etc. Statistical data show that 4G and 5G are fast, have high reliability, and the median latency of both is approximately 33 milliseconds.

When receiving an AGC signal, the EV aggregator will allocate and send the signal to each participating vehicle through wireless open communications; see Figure 3. A representative block is highlighted in yellow in Figure 4. This process might include multiple communication delays of different communication and measurement channels, processing times of the aggregator, response rates of the plug-in electric vehicle (PEV) batteries, and packet losses caused by imperfect network reliability. In open communication networks, the time delays and data packet loss are somewhat random, and their average behaviors depend on many factors, such as communication network capacity and transmitted distance. Note that Global Positioning System and location information might be needed for aggregators to determine which EVs are connected and which control areas (if there are more than one) a vehicle is currently connected to.
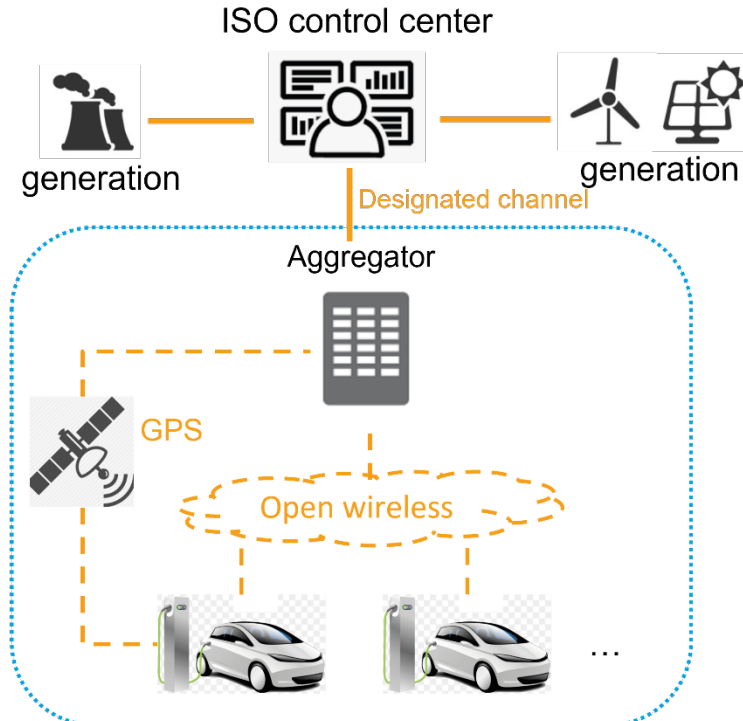
**Figure 3. Typical LFC system with EV aggregators**



→ Cyber variables with designated communication channels
→ Cyber variables with open communication networks
→ Physical variables
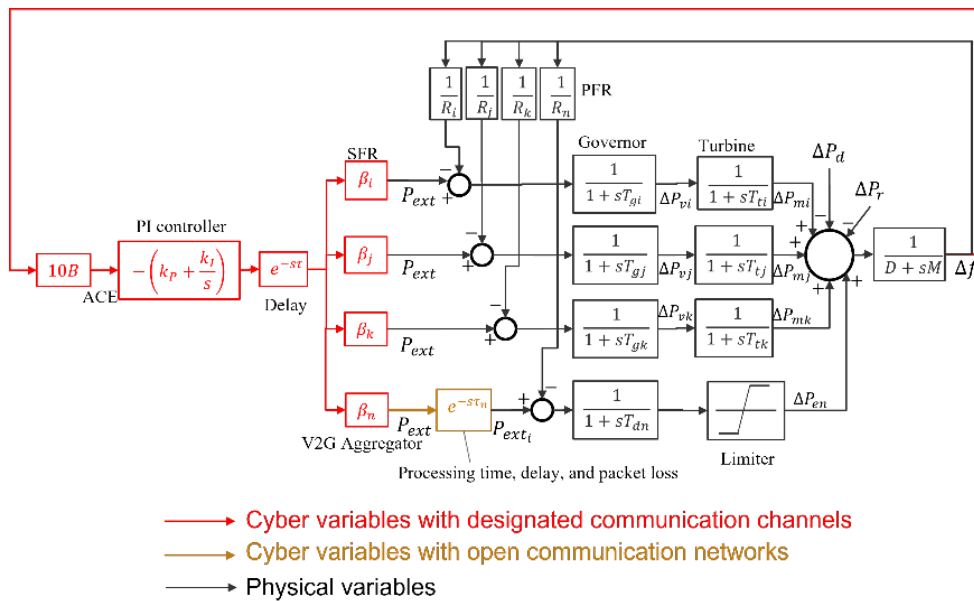
**Figure 4. LFC with communication considerations**

## 2.4  Co-Simulation Integration with HELICS

The HELICS co-simulation platform can accommodate the aforementioned simulators of multiple time domains; the synchronization of the simulation time among different simulators is implicitly controlled by a broker, and the information exchanges are realized by either subscriptions/publications or end point communications depending on if the federates represent

physical networks or communication networks. [38]. The schematic structure is shown in Figure 5. The HELICS command line interface (helics-cli) can be used in a terminal script to launch the co-simulation (e.g., running all the simulators simultaneously) [38]. Note that the communication variations regarding both the latency and packets dropping can be modeled in the end points; therefore, the cyber-physical interaction can be simulated in this platform as well. The co-simulation platform includes HELICS, ANDES, and OpenDSS. All are open-source packages/software; thus, the proposed T&D frequency dynamic co-simulation platform can be used without any commercial license limitations.
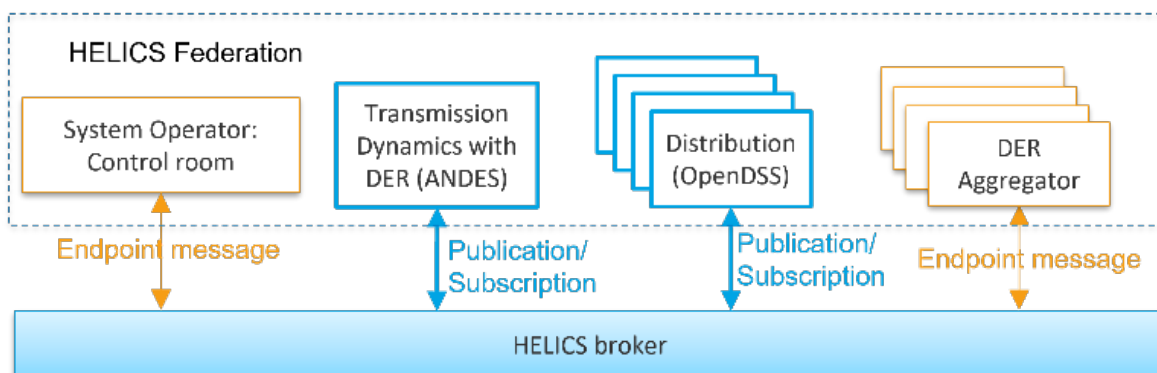


**Figure 5. Co-simulation framework structure in HELICS**

To efficiently build the co-simulation platform for large T&D systems, the platform code generation flow is described (with snippet demonstrations) as follows:

- Read the user-defined specifications for the simulation scenarios, which can be defined in a json file, as shown in Listing 1.
- Create the project directory with hierarchical subdirectories to include multiple simulation files, as demonstrated in Figure 6.
- Create the json files (shown in Listing 1) for the different simulators based on the specification information and copy them to the corresponding directories.
- Copy the predefined simulator template files for the specific simulators (transmission dynamic simulation using ANDES and distribution power flow using OpenDSS) to the corresponding directories. The simulator template file example is shown in Listing 2.
- Create the HELICS runner file for starting the federation with the command line interface. The runner file example is shown in Listing 3.

11
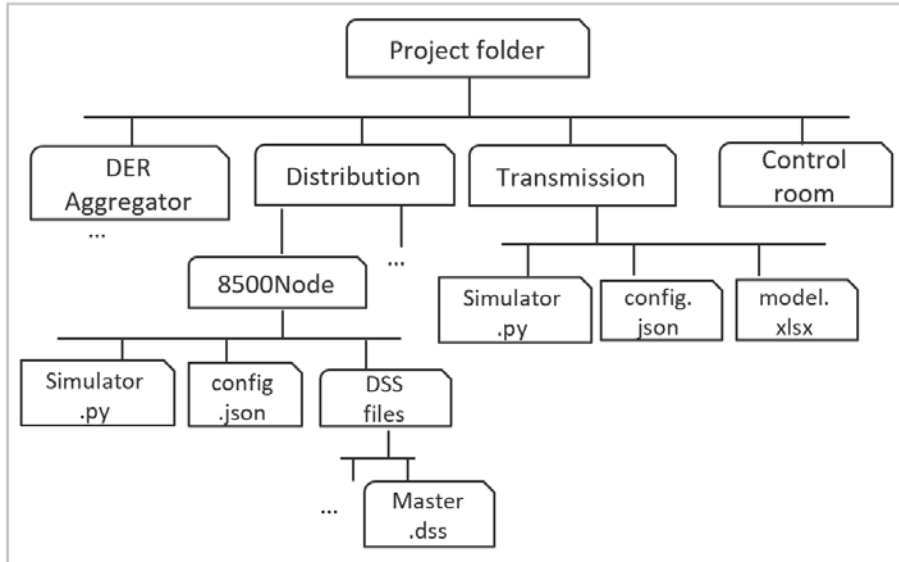
**Figure 6. Project directory demonstration**

The HELICS json file example is shown in Listing 1, with the following remarks:

- Line 1 and 9 declare the T&D networks.
- Line 2 and 10 define the names of the T&D networks. The IEEE 14-bus system and 8,500-node feeder are examples of T&D networks.
- Lines 3–5 define the transmission buses and the distribution feeder mapping.
- Lines 6–8 define the PQ load in the transmission network. Other T&D network parameters can be included in this file as well.

```
1.    {"Transmission": {
2.        "name": "IEEE14bus",
3.        "HV_MV_bus_map": {
4.         "4": "34Bus",
5.         "9": "8500Node"},
6.        "HV_PQ_index_map": {
7.           "4": "2",
8.           "9": "5"},
9.    "Distribution": {
10.        "name": "8500Node",
11.   …}
```

**Listing 1. HELICS json file example**

The HELICS simulator template Python file example is shown as pseudo-code in Listing 2:

- Line 1 reads the simulation parameters from the specific simulator's json file.
- Line 2 declares the federate execution start.
- Line 3 defines the subscription and publication variables with other federates.
- Line 4 loads the appropriate network data.
- Line 5 declares the HELICS execution start.

12

- Lines 6–11 define the time-based simulation with information exchange with other federates through either subscriptions/publications or end point communications.
- Lines 12 and 13 save the simulation results and close the federate.

```
1.  Read config.json
2.  Start federate
3.  Define subscription and publication based on config file
4.  Load network model
5.  Start HELICS execution mode
6.  Time based simulation:
7.   Subscribe  interfacing  physical  variables  from  other
      federates
8.   Receive end point information from other federates
9.   Run system simulator for one time step
10.  Publish interfacing physical variables to other federates
11.  Send end point information to other federates
12. Save results
13. Close federate
```

**Listing 2. HELICS Simulator.py example**

The HELICS runner file is shown in Listing 3:

- Line 1 defines the HELICS broker.
- Lines 2–12 define the federates in the HELICS co-simulation.
- Lines 3–6 define the information of one federate (transmission), and lines 7–10 define one distribution feeder's information. If there are multiple feeders, each feeder's information should be added here separately.
- Line 13 defines the name of the co-simulation project.

More details about the listing example files can be found in the HELICS manual [38].

```
1.   {"broker": true,
2.    "federates": [
3.      {"directory": "./Transmission",
4.       "exec": "python -u TransmissionSim.py",
5.       "host": "localhost",
6.       "name": "TransmissionSim"},
7.      {"directory": "./Distribution/8500Node",
8.       "exec": "python -u 8500Node.py",
9.       "host": "localhost",
10.      "name": "8500Node"}
11.  …
12.    ],
13.    "name": "CPDS_Co-simulation_HELICS_Runner"
14.  }
```

**Listing 3. HELICS runner example**

Assume that the communication variations can happen each time whenever transmitting data are needed. In the developed framework, we add two filter functions in HELICS to each communication channel: delay filter and packet loss filter functions.

A delay filter function can keep a sending end point from sending the data until a preconfigured time is past and then pass on the data to the destination end point; this preconfigured time (read by a HELICS broker) can be a constant or randomly generated from a distribution, i.e., normal distribution. The normal distribution assumption is based on the information in [45]. This setup can model a constant or time-varying delay for different communication channels.

In addition, each data packet transmit event has a chance of losing the packet (e.g., caused by hardware failure), resulting in the data packet either successfully passing or failing to pass. These events are naturally modeled as Bernoulli distributions and are parameterized by a single variable, p, the probability of a packet loss, with p in [0,1]. Inside HELICS, the added packet loss filter function can remove the packet data probabilistically and not send it to the destination end point. Note that we allow different values of p for different communication channels.

# 3 Modeling T&D Frequency Dynamics with DERs for AGC

This section describes the T&D network dynamics with DERs respecting local voltage constraints for AGC services. The dynamic model of DPV is shown in Figure 7. More details about the parameters in this model can be found in [49]. Unlike existing models in [49], a limit for the photovoltaic (PV) units' maximum available power, $P_{mppt}$, based on maximum power point tracking (MPPT) and other limits, is added to capture the PV's real-time total power output limitations because of the solar irradiation because the DPV frequency response will be constrained by its available headroom and local voltage limits. These maximum power limits should be considered. In the simulation, $P_{mppt}$ will be a time-series input (the resolution is 1 second) based on the available DPV power output.
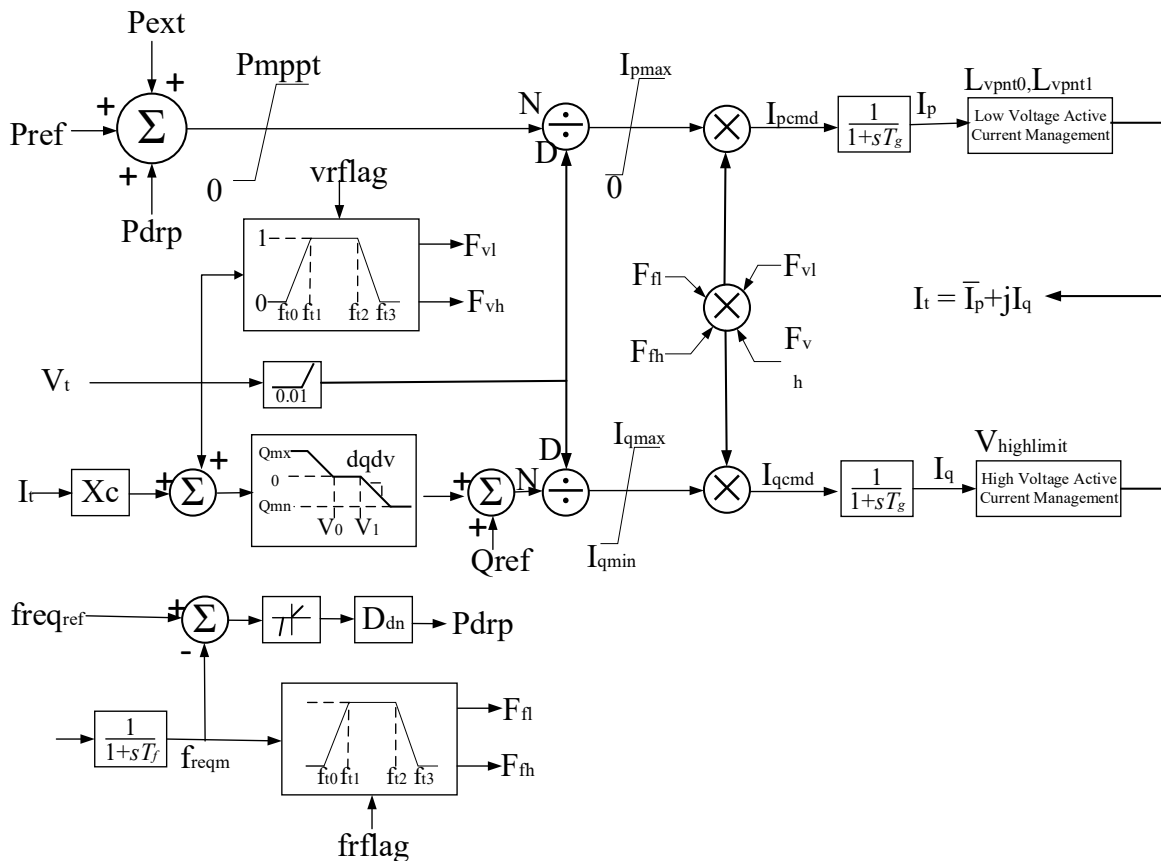


**Figure 7. DPV power plant generic model**

In Figure 7, $P_{ref}$ is the reference power determined in the generation scheduling model, updated every 5 minutes, which is obtained from the system operator's real-time economic dispatch. Its value is kept constant in the 5-minute interval. $P_{drp}$ is the PFR power output from the droop response. $P_{ext}$ is the SFR power set point, which is obtained from the system AGC control signal every 4 seconds. The total active power output of $P_{ref}$, $P_{drp}$, and $P_{ext}$ should not exceed the PV's maximum available power, $P_{mppt}$. This will be introduced with more detail in the

following subsections. Some parameters will be introduced in the following subsections, and others shown in Figure 7 are explained in [49].

## 3.1 DER Frequency Response Modeling

### 3.1.1 Droop Control for PFR

The dynamic model of DPV shown in Figure 7 includes the droop control for PFR. When the frequency drop is larger than the PFR deadband, the DPV will change its active power output accordingly. An additional power output, $P_{drp}$, will be included for its PFR:

$$P_{drp} = \begin{cases} \frac{(f_0 - db_{UF}) - f}{60} D_{dn}, f < f_0 \\ \frac{f - (f_0 + db_{OF})}{60} D_{dn}, f > f_0 \end{cases} \tag{4}$$

where $f_0$ is the reference frequency (60 Hz in North America); $db_{UF}$ and $db_{OF}$ are the underfrequency and overfrequency deadband; and $D_{dn}$ is the per-unit power output change to 1 per-unit frequency (frequency droop gain).

### 3.1.2 SFR through AGC

As shown in Figure 8, SFR is enabled by an AGC model that includes two components: an area-level model that calculates the ACE from (5) in Figure 8 and a plant-level control model that receives the ACE signal and sets the reference power, $P_{ext}$, for each plant. For simplicity, assume there is one area in the simulation and no interchange with other areas, according to the North American Electric Reliability Corporation [50], [51], ACE is defined as, with the interchange metering error ignored, i.e.:

$$ACE_{tt} = 10B\left(f_{reqm,tt} - f_0\right) \tag{5}$$

where $tt$ is the AGC time interval index; $ACE_{tt}$ is the ACE at the AGC interval $tt$; $f_{reqm,tt}$ is the measured system frequency at the AGC interval $tt$; $f_0$ is the system reference frequency (60 Hz); and B is the frequency bias in MW/0.1 Hz. A positive ACE means the system is over generating power, whereas a negative ACE means the load is larger than the generation. In this paper, a frequency error tolerance deadband, fdb, is introduced to eliminate the unnecessary movement of the generation set points. A proportional integral (PI) control is applied to the ACE signal to generate the actual control signal that will be passed on to individual generators. $K_p$ and $K_i$ are the coefficients of the PI controller.
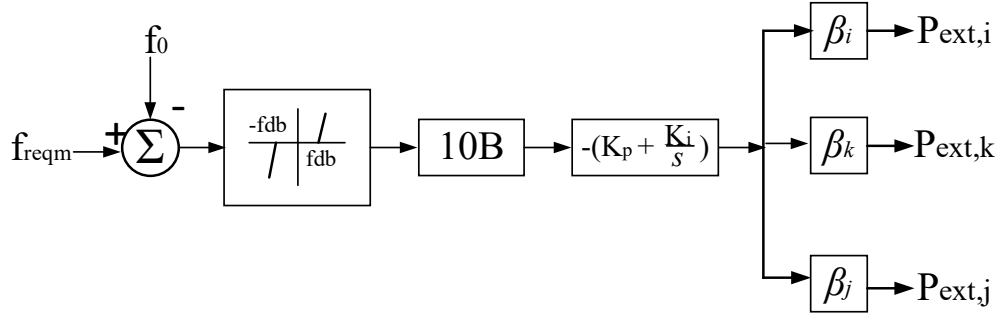
**Figure 8. AGC model**

The ACE signals are updated every 4 seconds to represent their discrete nature in the field. The ACE signals are then passed on to each AGC generator considering the unit's participation factor so that the individual AGC power plant's SFR power, $P_{ext}$, is updated accordingly, as input in the DPV model, as shown in Figure 7. The participation factor of each unit's AGC response is decided by the real-time economic dispatch through the energy and regulation reserve co-optimization, as shown in Figure 8; $\beta_i$ is the i-th unit's participation factor. Because this project focuses on the T&D dynamic co-simulation, how to calculate this participation factor is omitted. In real operation, this participation factor is optimized in real-time economic dispatch considering the renewable and load variations [52]–[55].

## 3.2 Combination of DER Dynamic and Static Models

Note that the DER dynamic model is included in the transmission simulator so that the frequency dynamic responses of the DERs—both PFR and SFR—can be accurately included in the transmission frequency dynamic simulation. Most DERs are hosted in distribution systems, where the local voltage needs to be maintained in the range from 0.95–1.05, along with distribution line rating limits. To account for these local requirements, DER static power flow models are also considered in the distribution simulators. This treatment is then completed by adjusting the overall power injection/withdraw at the substation from the distribution simulators, as in:

$$S_i^{abc} = S_{i,with\ DER}^{abc} + \sum S_{i,DER}^{abc} \tag{6}$$

where $S_{i,with\ DER}^{abc}$ is the distribution abc three-phase net load (the substation power), considering the DER power outputs at individual distribution nodes (the distribution feeder is connected to transmission bus i); and $S_{i,DER}^{abc}$ is the DER power outputs in the abc three phases. $S_i^{abc}$ is then converted to the positive-sequence power using Eq. (6) and sent to the transmission simulator. Through this treatment, the DER power is simultaneously modeled in both the transmission and distribution networks.

### 3.2.1 Transmission Frequency Dynamic Simulation with DER Dynamic Models

The transmission system frequency dynamic simulation is performed with ANDES, an open-source, Python-based dynamic simulation library [56]. ANDES used a hybrid symbolic-numeric framework for the system electromechanical dynamic modeling and simulation. The system dynamics can be modeled as a set of mass-matrix differential algebraic equations [57]:

$$M\dot{x} = f(x, y, u) \tag{7}$$

17

$$0 = g(x, y, u) \tag{8}$$

where $f$, $g$ are the differential and algebraic equations, respectively; $x$, $y$, and $u$ are the state, algebraic variables, and inputs; and $M$ is the mass matrix. Here the bold font represents matrix or vectors. The DPV dynamic model shown in Figure 7 is added to ANDES to simulate the DPV frequency dynamics [58]. The frequency deviation and ACE from the dynamic simulation are sent to the turbine governor and DER aggregators. Other DER dynamic models, such as distributed energy storage, are also available in ANDES.

### 3.2.2 Distribution QSTS Power Flow Simulation with DER Static Model and Headroom Estimation

The distribution system QSTS power flow simulation is performed with OpenDSS. To account for the local voltage constraints that might be incurred by the DER frequency dynamic response, the active power outputs of the DERs are modeled in the distribution systems as well. As discussed in Subsection II-C, this will ensure that the DERs respect the local constraints and fit into the overall co-simulation framework.

For DERs to provide frequency response, at a certain time step, distribution system operators or DER aggregators submit the DER headroom to the transmission system operators. This headroom is estimated through a fast (linear) optimization scheme, as in (9)–(12). The objective function (9) maximizes the total output of DERs in a specific distribution system while respecting local constraints, including voltage and thermal limits (11), (12), as well as an equality constraint (10) of the precalculated voltage-power sensitivity matrix (VSM, denoted by JVSM), which can be seen as power flow equations linearized at certain system states. VSM is obtained based on the method introduced in [59], but here it focuses only on the DER nodes and active power. The VSM is obtained by perturbing the power injections at nodes that are connected with DERs, one at a time, until exhausting all the DER nodes:

$$\max(\mathbf{1}^T \boldsymbol{P}_{DERs}) \tag{9}$$

$$\text{s. t. } \boldsymbol{J}_{VSM} \Delta \boldsymbol{P}_{DERs} = \Delta \boldsymbol{V} \tag{10}$$

$$\underline{\boldsymbol{V}} < \boldsymbol{V}_{base} + \Delta \boldsymbol{V} < \overline{\boldsymbol{V}} \tag{11}$$

$$\underline{\boldsymbol{I}} < \boldsymbol{I} < \overline{\boldsymbol{I}} \tag{12}$$

where $\boldsymbol{1}$ is a column vector with all elements being 1; $\boldsymbol{P}_{DERs}$ is a column vector with size $m{\times}1$ that contains the $m$ DER outputs; $\Delta \boldsymbol{P}_{DERs}$ represents the change in the active power outputs of the DERs; $\Delta \boldsymbol{V}$ represents the change in voltage at all nodes (assume $n$ nodes) in the feeder; $\boldsymbol{J}_{VSM}$ denotes the sensitivity matrix with size $n{\times}m$; $\boldsymbol{V}_{base}$ is the base voltage values of all nodes from the current time step; and $\boldsymbol{I}$ represents the current flow in the circuits.

The output from this optimization scheme is used to calculate the total maximum headroom by (13), then it is sent to the transmission system simulator to decide the available headroom of the DERs for frequency regulation:

$$P_{headroom} = max(\sum \boldsymbol{P}_{DERs}) - \sum \boldsymbol{P}_{DERs}^{Base} \tag{13}$$

18

where $P_{DERs}^{Base}$ is the DER output at the current time step. The transmission system simulator then considers these limits, which are shown in (14):

$$P_{DER} = min\ (P_{DER}^{PFR} + P_{DER}^{SFR} + P_{DER}^{Base}, P_{mppt}, P_{caps} \ P_{DER}^{Base} + P_{headroom}) \qquad (14)$$

where $P_{caps}$ denotes the capacity ratings for the DERs; therefore, with (14), the DER frequency response will respect both the transmission dynamic response and the distribution voltage limitations. Note that the DER headroom evaluation in this subsection is performed every 10 seconds in the co-simulation to reduce the co-simulation computational burden, which can be adjusted based on the system settings and preferences.

# 4 Case Studies for T&D Dynamic Co-Simulation Model Validation

In this chapter, to illustrate the effectiveness and efficiency of the proposed framework, three systems representing different T&D network sizes are used. First, a small validation system is assembled from the IEEE 14-bus transmission system [36] and IEEE 13-bus test feeder for benchmarking. Next, the proposed co-simulation connects the IEEE 14-bus transmission system with two detailed distribution feeder models. Then, the IEEE 39-bus system is tested with all 19 load buses connecting various distribution feeders. Last, a large system of the Texas 2,000-bus network [60], [61] connected with 243 distribution feeders [62], is tested. This demonstrates the superiority of the framework in computational performance. The testing simulations are performed on a personal laptop with Intel CORE i7 as the central processing unit in the small and midsize case studies; the large case is performed on the high-performance computer (HPC) Eagle at the National Renewable Energy Laboratory (NREL) [63], i.e., 96-GB memory, 18 cores of 3.0 GHz. The Python version is 3.7.
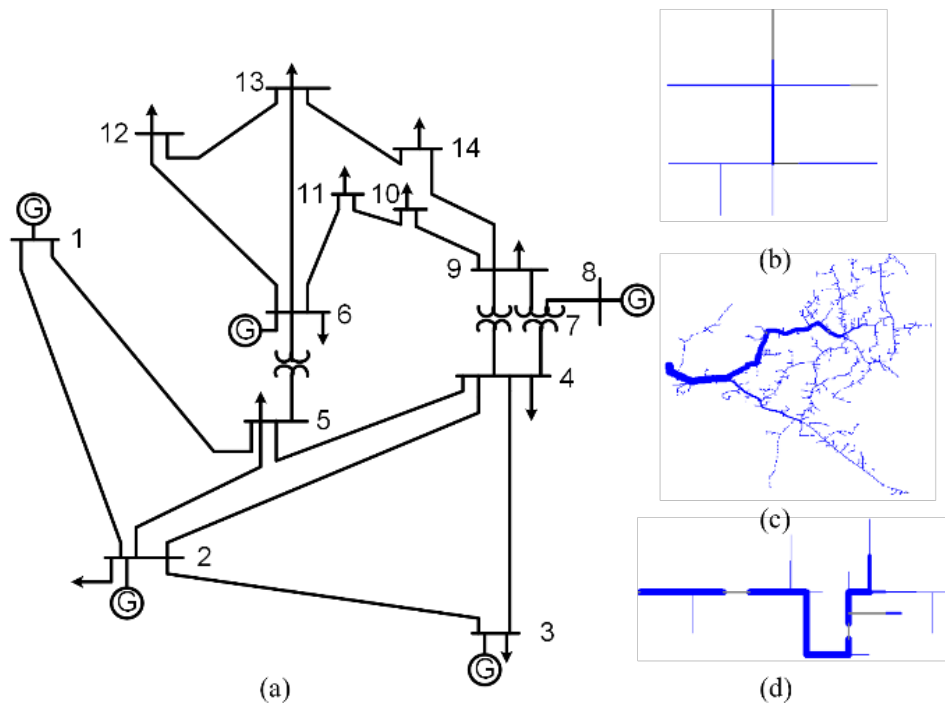


**Figure 9. Integrated T&D network with IEEE 14-bus system: (a) IEEE 14-bus transmission system, (b) IEEE 13-bus feeder used for validation, (c) IEEE 8,500-node feeder, and (d) IEEE 34-bus feeder**

## 4.1 IEEE 14-Bus System

### 4.1.1 Validation of the Proposed Co-Simulation Framework Against Integrated System

To validate the accuracy of the proposed T&D dynamic co-simulation framework, an integrated T&D network is created from the IEEE 14-bus system and the IEEE 13-bus feeder positive-sequence model (converted from the original version of the OpenDSS IEEE 13-bus distribution feeder); see Figure 9 (a) and (b). The integrated system consists of 26 buses in ANDES format

(the distribution feeder head bus is Bus 11 in the IEEE 14-bus transmission network). Four DPV units with 0.5-MW power output are added to the distribution system (connected to busses 632, 633, 646, and 671 of the 13-bus feeder). It is assumed that four DPV units provide 10% of the total AGC response, with each DER providing 2.5% of the AGC response. The other conventional generation units provide 90% of the AGC response, which is evenly distributed among five conventional generation units. A generation trip scenario is simulated for this integrated network as a benchmark for comparison. Gen 3, with 40-MW power output, is tripped at 10 seconds. The same scenario is also simulated using the proposed co-simulation framework. Figure 10 compares the voltage, frequency, and DER output profiles for the two simulations: the *integrated-sim* means that the integrated T&D networks are simulated in ANDES as one network. The *co-sim* represents the results from the proposed T&D dynamic co-simulation.

Figure 10 shows that the dynamic responses of the bulk system frequency, the voltage, and the DER power output from the integrated T&D network simulation and the proposed T&D dynamic co-simulation are very close. This demonstrates the accuracy of the proposed T&D dynamic co-simulation framework. The frequency and voltage profiles from the proposed co-simulation model can accurately capture the T&D network dynamics during the system transients.



(a)

(b)

(c)
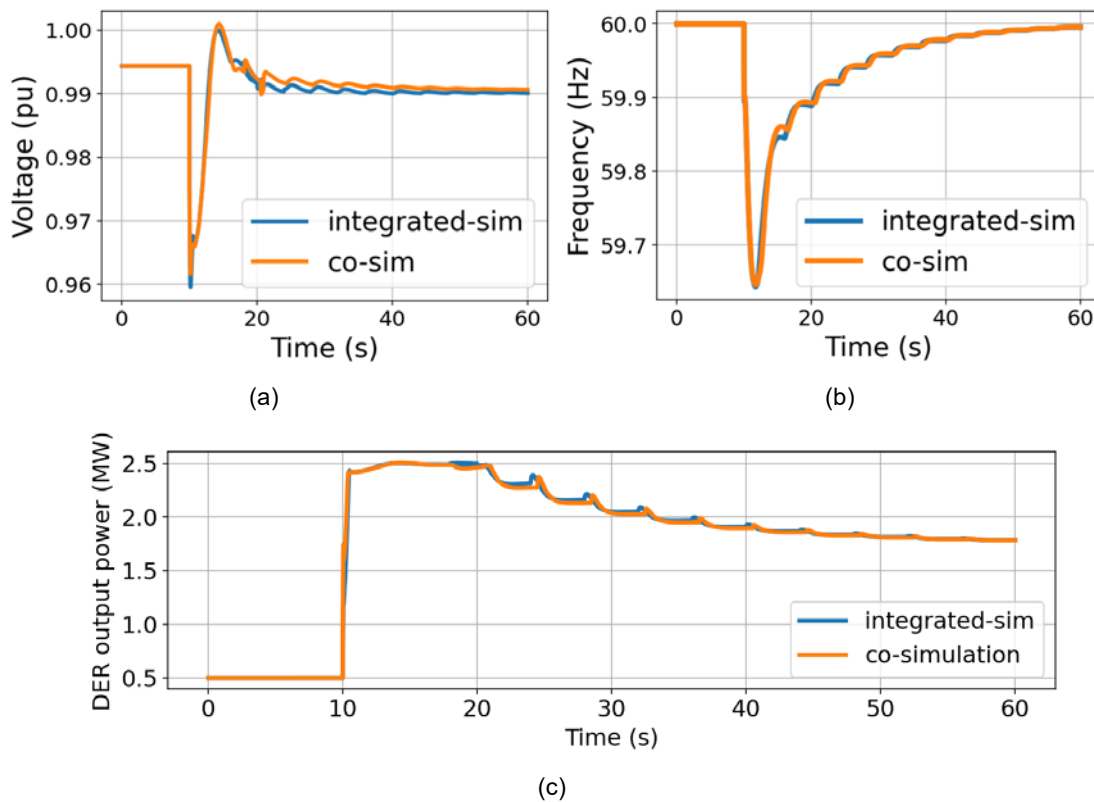
**Figure 10. Comparison of the integrated T&D network simulation and the proposed co-simulation: (a) voltage response, (b) system frequency response, and (c) DER power output under the generation drop case**

### 4.1.2 Co-Simulation with Two Distribution Feeders

The T&D network consists of the IEEE 14-bus system and two distribution feeders [64], as shown in Figure 9 (a), (c), and (d), with Bus 4 connected with the IEEE 34-bus feeder, and Bus 9

21

connected with the IEEE 8,500-node feeder. Each feeder hosts 10 DPV units with nameplate ratings of 900 kVA. Each feeder has an aggregator coordinating the DPV AGC response in its own distribution feeder. The dispatched active power outputs of the DPV are assumed to be 500 kW for the simulated time of 60 seconds. The transmission dynamic parameters can be found in [36]. Gen 5 in the original IEEE 14-bus system reduces its power output from 35 MW to 25 MW to accommodate the total active DER power output, which is 10 MW, with 0.5 MW for each DER. Here, for simplicity, all DERs are assumed to be DPV; other types of DERs can be modeled as well.

### 4.1.3 DER AGC Response with Load Variation

This subsection studies the performance of the SFR of the DPV in the proposed co-simulation model under random load variations mimicking normal operation conditions. It is assumed that loads vary randomly with a 2% standard deviation in the simulated time horizon. In this scenario, the system sends the aggregated AGC control signal to each aggregator, then the aggregators disaggregate the AGC signal to individual DERs with a 4-second interval. Because the participation factors of the AGC response are normally decided by the real-time economic dispatch, which is not in the scope of this co-simulation model, it is assumed that 20 DPV units provide 10% of the total AGC response, with each DER providing 0.5% of the AGC response. The other conventional generation units provide 90% of the AGC response, which will be evenly distributed among five conventional generation units.

Table 2 summarizes the statistical metrics of the system frequency and ACE. The mean frequency is close to 60 Hz. The standard deviation of the frequency is small. The maximum and minimum frequency deviation is within 0.065 Hz. This shows that the T&D system frequency performance is normal under the load variation. Figure 11 shows the system frequency and the probabilistic distribution of the frequency across the simulated time. The frequency varies mostly within a small range around +/- 0.05 Hz.

**Table 2. Statistics of Frequency and ACE**

| Item | Frequency (Hz) | ACE (MW) |
|------|----------------|----------|
| Mean | 59.999 | -0.172 |
| Std | 0.026 | 4.174 |
| Min | 59.936 | -10.371 |
| Max | 60.054 | 8.833 |

Figure 12(a) shows the DER AGC signal provided by the DER aggressors (one DER is plotted here). When the DERs do not provide SFR services, their AGC signal is zero. When the DERs provide SFR, their AGC signal will change based on the system ACE. This figure also shows that the DER AGC signal changes every 4 seconds. Figure 12(b) further demonstrates that the output of the DERs varies according to their AGC signals; this output also considers local voltage constraints that are based on the optimization scheme in Subsection III-C and the maximum available power of the DER (MPPT, DER capacity ratings). In this study, the DER Pmppt is a 1-second time-series input data (the blue dashed line). The maximum power from the VSM is calculated every 10 seconds (the green dashed line). Figure 12(b) shows that the DER output (the orange solid line)—including its SFR response—is less than Pmppt (decided by

22

irradiation), and the maximum value is limited by local voltage constraints (see VSM max); therefore, both the available power variation resulting from solar radiation intermittency and the local distribution voltage limits can be respected when DERs provide SFR to the transmission system.
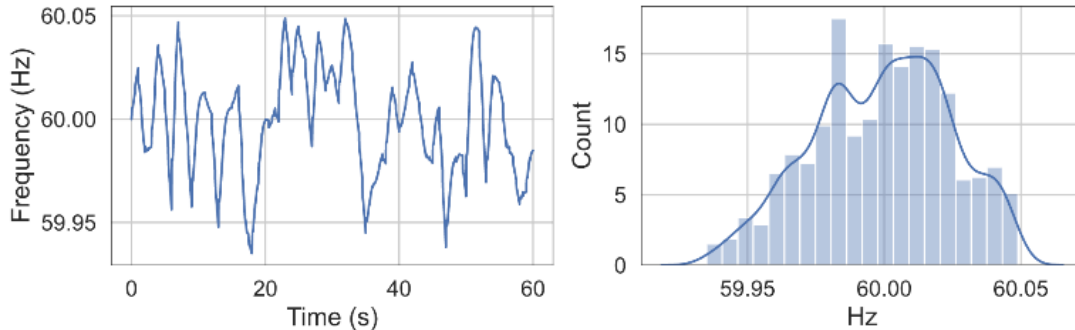


**Figure 11. System frequency and distribution**



(a)                                                      (b)
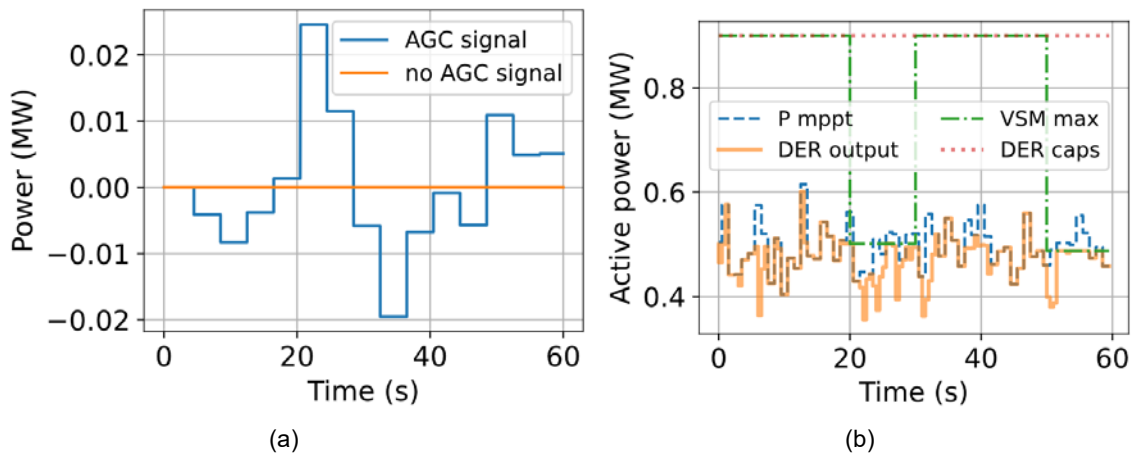
**Figure 12. (a) Example of one DER AGC signal from a DER aggregator and (b) example of the power output from one DER under the load variation**

Figure 13(a) shows the overall voltage profile for the 34-bus feeder (connected with Bus 4 of the 14-bus transmission network), and Figure 13(b) shows the 8,500-node feeder (connected with Bus 9 of the transmission network). The blue solid line shows the average voltage within the feeder, and the shaded area denotes one standard deviation from the average. The dashed lines mark the minimum and maximum values of the feeder voltages. It can be observed that the two feeder voltages are within approximately 0.95–1.05 p.u. when the system load varies; therefore, with DERs providing SFR services, the local voltage constraints are respected using the proposed T&D frequency dynamic co-simulation model.

23
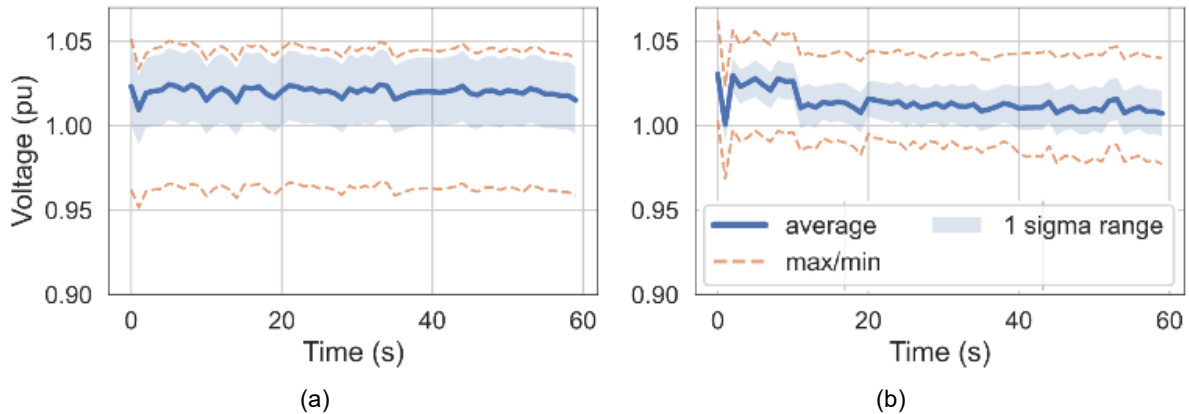
**Figure 13. Voltage plots of (a) 34-node feeder and (b) 8,500-node feeder**

### 4.1.4 DER PFR Under Generation Outage

The DER PFR is activated when the frequency deviates more than its PFR deadband (0.017 Hz in this study) presented through a generation trip scenario here. It is assumed that Gen 3, with 40-MW power output, is tripped at the fifth second. Similar to the previous subsection, 20 DERs provide 10% of the AGC response, with each DER providing 0.5% of the AGC response. The rest of the AGC is provided by conventional generation units. Note that the loads are kept constant in this case for clear presentation. The DER Pmppt varies near 0.8 MW (the blue dashed line in Figure 14).
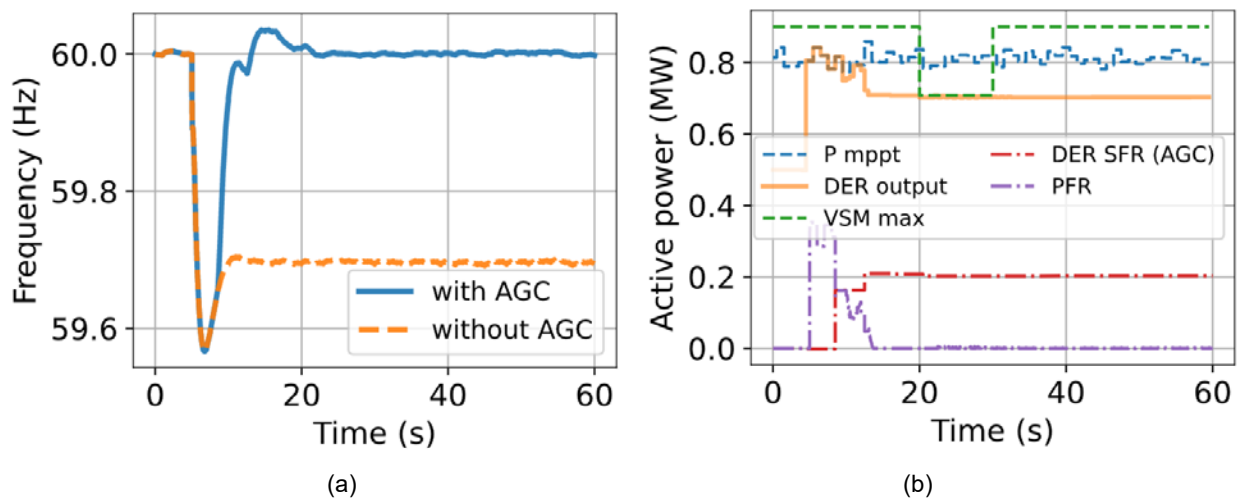


**Figure 14. (a) Frequency response with/without AGC and (b) DER power output, PFR, SFR, and its MPPT and VSM limits**

Figure 14(a) compares the system frequency dynamic response with and without the AGC response. As expected, the frequency does not recover to 60 Hz without the AGC (SFR), although it settles at a value less than 60 Hz. With the AGC enabled, the frequency is restored to 60 Hz. Figure 14(b)          (a)     (b)

Figure 14 demonstrates the DER's PFR and SFR after the generation outage, along with the DER's actual power outputs and limits, including $P_{mppt}$ and VSM max (the green dashed line). The total power output (the orange solid line) including the reference power (i.e., the DER's dispatched power output 0.5 MW), PFR (the purple dashed line), and SFR (the red dashed line) is less than its $P_{mppt}$ and VSM power limit; thus, these limits are respected during the dynamic

24

response of the DERs. This figure also demonstrates that after the generation outage, the DER's PFR responds first by increasing the DER's power output to support the frequency. Then the DER's SFR starts to increase the power output to stabilize the system frequency once the DER receives the SFR signal from the aggregator. After the SFR returns the frequency to a normal level, the PFR phases out. In this simulation, the SFR signal is sent every 4 seconds; thus, the SFR kicks in at the eighth second. Figure 15 shows the voltage behavior of two feeders in this case. After the fifth second, both feeders experience voltage dips after the generation outage, followed by small voltage overshoots that mainly result from the DER and conventional generation unit frequency responses. The fact that all these behaviors are captured shows the effectiveness and accuracy of the proposed framework.
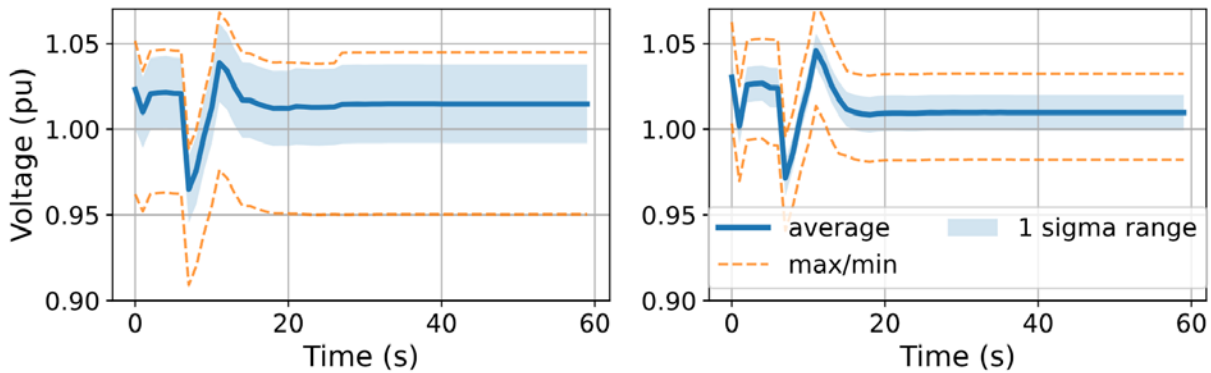


**Figure 15. Voltage response of (a) 34-bus feeder and (b) 8,500-node feeder**

## 4.2  Texas 2,000-Bus Co-Simulation

To demonstrate the scalability the proposed T&D dynamic co-simulation model, the Texas 2,000-bus synthetic transmission network is used. This system has 67 GW of load and 98 GW of total generation capacity, which is built on the footprint covering most of the U.S. State of Texas [60], [61] (see Figure 16 (a)). The distribution network consists of 243 feeders, which is a subset of the Austin synthetic feeder data set from [65], [62]; this data set covers the geographic area of Austin, Texas (see Figure 16 (b)). These distribution feeders replace 2.83 GW of load in 39 substations in the Austin area in the transmission network. There are a total of 360,000 loads and 1,000,076 electrical nodes in the distribution system. There are 8,400 DPV units connected to these feeders (200 DPV units at each of 36 substations and 400 DPV units at each of the remaining 3 substations). The total DPV power output is 222.7 MW, and the total installed DPV capacity is 2.1 GW. The co-simulation was performed on the HPC Eagle at NREL [63]. At 11 seconds, the generator at Bus 6078 with 477-MW output is tripped. The SFR is provided only by the connected DPV in this system. The voltage profiles, system frequency, and DER power outputs following this generation outage event are shown in Figure 17. Because it takes longer to restore the frequency to its nominal level, a 160-second co-simulation is performed for this large system.
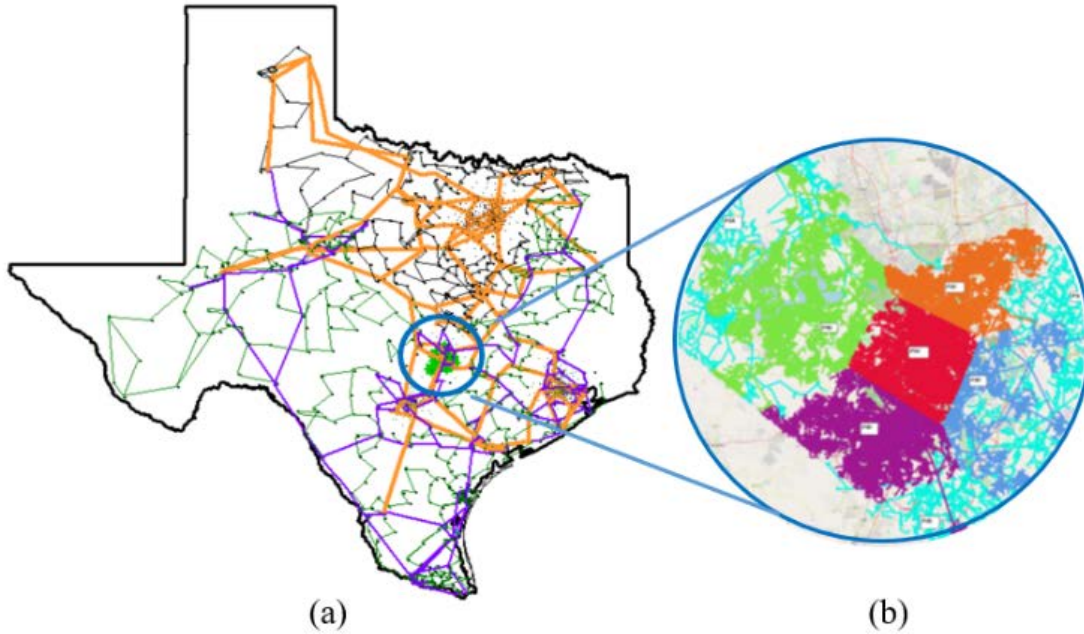
**Figure 16. (a) One-line diagram of the 2,000-bus case [60], with the Austin area marked in green, and (b) five subregions in the distribution Austin data set [65]**
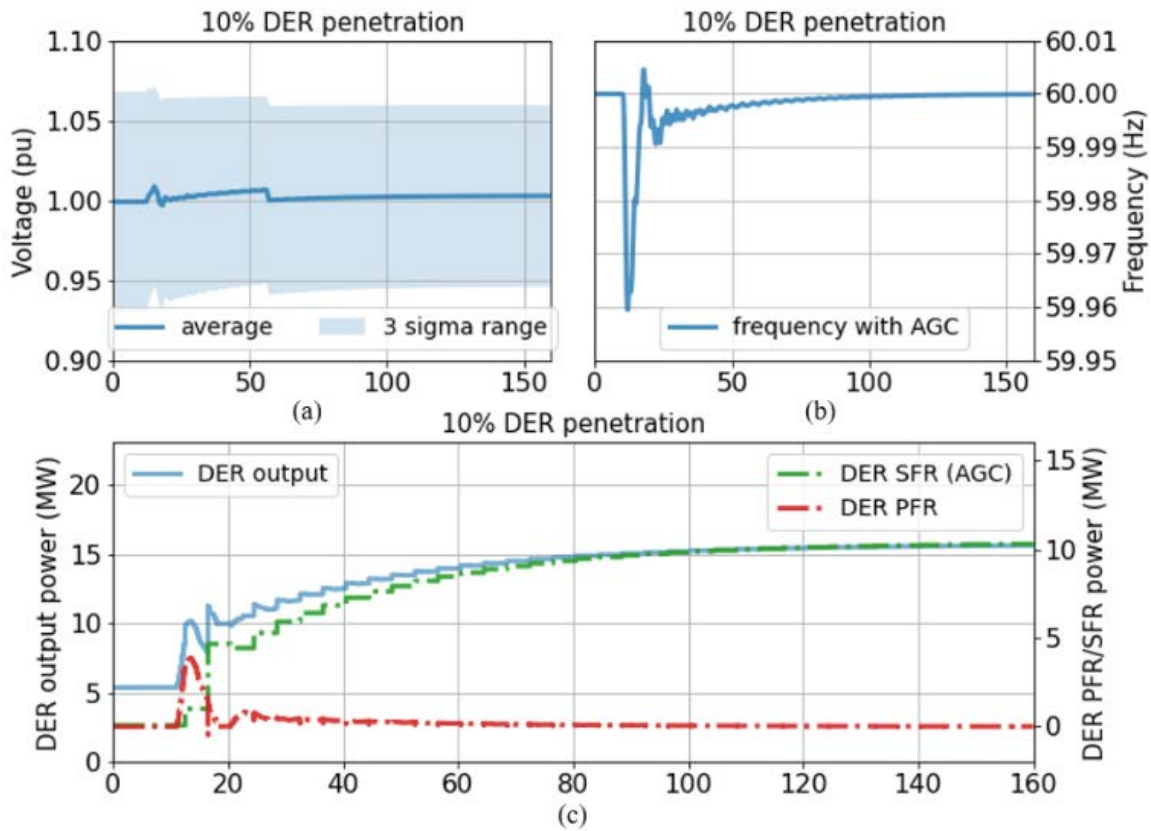


**Figure 17. Representative co-simulation results of the 2,000-bus case: (a) voltage profiles of a substation bus connected with distribution feeders; (b) system frequency response; and (c) DER power output, PFR, and SFR**

As shown in Figure 17, DERs provide both PFR and SFR after the generation outage. In Figure 17(a), the local distribution voltage increases with the increasing DER power output to support the system frequency. When the local voltage increases, the voltage regulator could be activated to reduce the voltage, depending on the setting. This shows that the proposed T&D dynamic co-simulation model can capture both the transmission frequency and the distribution network voltage dynamics. Figure 17(b) shows that the system frequency drops following the generation outage and is gradually restored to the nominal value with the support of the PFR and SFR of the DERs. (Note that the traditional generation in the system also provides PFR.) The DER power output is shown in Figure 17(c), similar to the results in the previous subsections. After the contingency, the PFR is activated first, then after the SFR signal is received, the SFR increases the DER power output, and the PFR gradually phases out. When the frequency is stabilized, the PFR reduces to 0, and the SFR reaches the stable level. In this large system, it takes longer to stabilize the frequency after the contingency than in previous smaller systems.

## 4.3  Computational Performance

Besides HELICS (parallelly running separate federates), the treatment of the DER models in the proposed co-simulation framework enables the efficient and accurate simulation of the DER frequency dynamic response in the large-scale T&D co-simulation environment. In the case studies, for the validation case, the integrated system simulation takes 50 seconds, whereas the co-simulation takes a comparable 46 seconds on a personal laptop with Intel Core i7-10610-U processor; for the IEEE 14-bus system with 34-bus and 8,500-node T&D networks, the 60-second dynamic simulation takes approximately 60 seconds on the same machine. For the IEEE 39-bus system with 19 distribution feeders—including several large-scale feeders, including two 8,500-node distribution feeders and the EPRI-J1 distribution feeder (containing 4,200 nodes)—the 60-second time domain T&D co-simulation takes approximately 3 minutes on the same machine. The case studies show that as the framework incorporates more detailed feeders, the computational time does not increase linearly. For the 2,000-bus co-simulation, performed on the HPC, the 160-second simulation takes approximately 48 minutes; therefore, for the large T&D co-simulation, the proposed T&D dynamic co-simulation model can be efficiently run on the HPC with relatively low cost. In terms of building the proposed co-simulation platform, an automated co-simulation model development process is designed for large-scale T&D co-simulation to set up T&D co-simulation files in HELICS. Note that in general for T&D co-simulation, it can take several seconds to synchronize all the physical variables in T&D networks at the beginning of the co-simulation. In all testing cases, the actual simulation starts after the T&D physical variables are synchronized in the T&D networks in the framework.

# 5 Use Case 1: Delay Margin of SFR by DERs

Unlike conventional generators, which use a dedicated communication channel to provide AGC [32], DERs can use open communication networks to exchange control signals with system control centers, possibly through DER aggregators [33]. The open networks expose several vulnerabilities of the DER AGC services, such as extended communication latency, increased packet loss, and cyberattacks (e.g., false data injection); therefore, it is imperative to study the impact of the communication variations in DER AGC on the system frequency stability to ensure reliable operation of the future electric grid with high penetrations of DERs. Although it depends on the specific communication infrastructure, normal time delays—ranging from several tens to hundreds of milliseconds—are introduced in transmitting and processing remote signals [34], [35]. These delays will likely increase when open communication networks (e.g., mobile or fixed broadband) and multilayer structures (DER aggregators) are introduced, especially during periods of congested communications because of the large amount of data exchanged.

Existing research on the communication delay in LFC focuses on conventional generators. Reference [66] designs a delay-dependent LFC (to find the parameters for the PI controllers) for time-delay power systems. In [67] and [68], linear matrix inequalities are used as the stability criteria to design PI controllers and to find the delay margin of the system, respectively. Reference [69] discusses the impact of a transmission delay and the sampled control signal on the system stability because the AGC signals are updated every few seconds in the field. Reference [70] investigates the impact of the discrete secondary controllers on the dynamic response of power systems and discusses the analogy between AGC and real-time electricity markets.

The existing research studying AGC with delays and system frequency stability is based on traditional modeling of the state-space representation and Lyaponuv theory for AGC and an aggregate manner of simulation (e.g., total inertia in Simulink) with rather simplified test systems. Further, the current delay margin evaluation methodology might not be well suited for DER AGC control analysis, with multilayer, open communication networks and discrete control signals.

This section studies the impact of the communication delay on DER AGC and system frequency stability. In particular, the delay margin of DER AGC is calculated based on the proposed framework.

## 5.1 DER LFC with Delays

LFC from DERs with delays is shown as a block diagram in Figure 18. It combines PFR and SFR with added delay blocks from a system-wide perspective. The red lines and blocks represent the cyber variables where communications are required, whereas the black represents the physical variables (governors, turbines, inverters) and locally controlled PFR. This synthesis of LFC with delays can also be analytically expressed as state-space equations. First, the following state and output vectors are defined, as in (15) [68], [71]:

$$
\begin{aligned}
x(t) &= [\Delta f \quad \Delta P_m \quad \Delta P_v \quad \int ACE]^T \\
y(t) &= [ACE \quad \int ACE]^T
\end{aligned}
\tag{15}
$$

28

where $\Delta f$ is the system frequency deviation; $\Delta P_m$ is the conventional generator mechanical power deviation; $\Delta P_v$ is the valve/gate position change of the governor; and $\int ACE$ is the integral of the ACE. The control signal with the PI controller is written as shown in (16):

$$u(t) = -K_P ACE - K_I \int ACE. \qquad (16)$$

Therefore, the delayed LFC state-space equations are shown as in (17) [71]:

$$\begin{cases} \dot{x}(t) = Ax(t) + Bu(t) + A_d x\big(t - d(t)\big) \\ \qquad\qquad + B_h u\big(t - h(t)\big) + Fw(t) \\ y(t) = Cx(t) \end{cases} \qquad (17)$$

where $d(t)$ and $h(t)$ are the time-varying delay amounts in the state and control input vectors; $w(t)$ is the system disturbance (e.g., load or generation change); A, B, C, which are normally assumed to be known, are the state matrix, control matrix, and output matrix, respectively; F is the perturbation matrix; and $A_d$ and $B_h$ are the state matrix and control matrix but describe the relationship with the previous state and control vectors. For example, the previously calculated control vector, $u\big(t - h(t)\big)$, affects the current state, $x(t)$. Note that because the PI controller is included in (17), it is also called a static output feedback control problem ($K_P$, $K_I$ are constants) [71]. In this section, (17) serves as the exposition of the delayed control system.
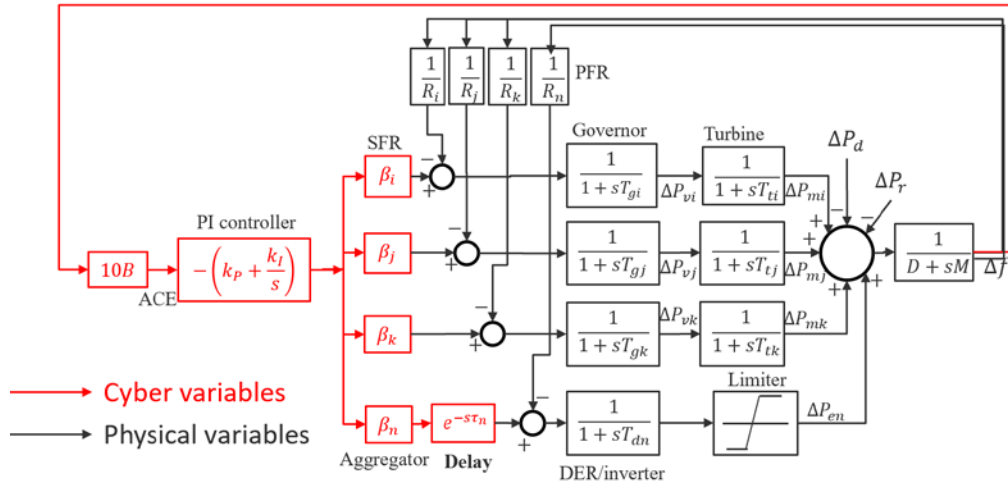


**Figure 18. Schematic model of the cyber variables (red) with delays and the physical parts in the transmission system (black)**

## 5.2  System Setup (Transmission-Communication Systems)

Assume that the overall system comprises a transmission system dynamic simulator; a control center; turbine governors of conventional generators; and a DER aggregator for each load bus, including DPV or other DERs, as shown in Figure 19.
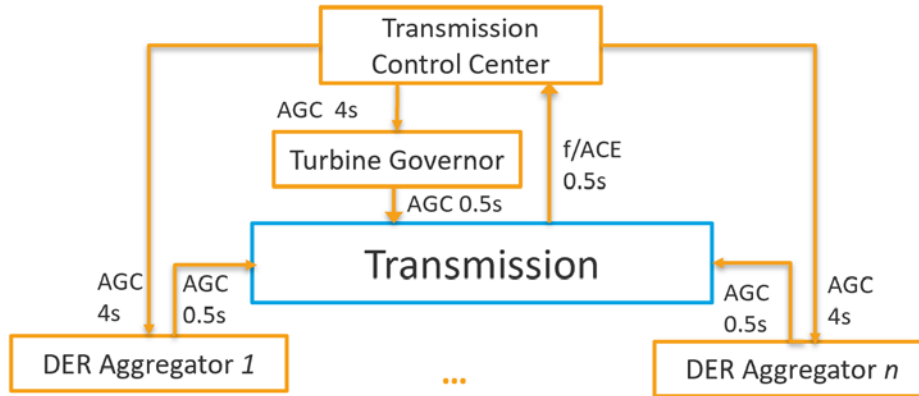
**Figure 19. Simulation components with information exchange**

The IEEE 39-bus system shown in Figure 20 is used to evaluate the impact of the communication delay on the DER AGC signals. In this study, DPV is used to represent the DERs. Other DERs can be added as well. Assume the following system operating condition: 40 DERs at every load bus, for a total of 19 load buses with 760 DERs; the generation of the DERs is 20% of the loads at every load bus, and they are distributed evenly. The DER frequency dynamics with PFR and SFR have been added in ANDES, as described in Section II.
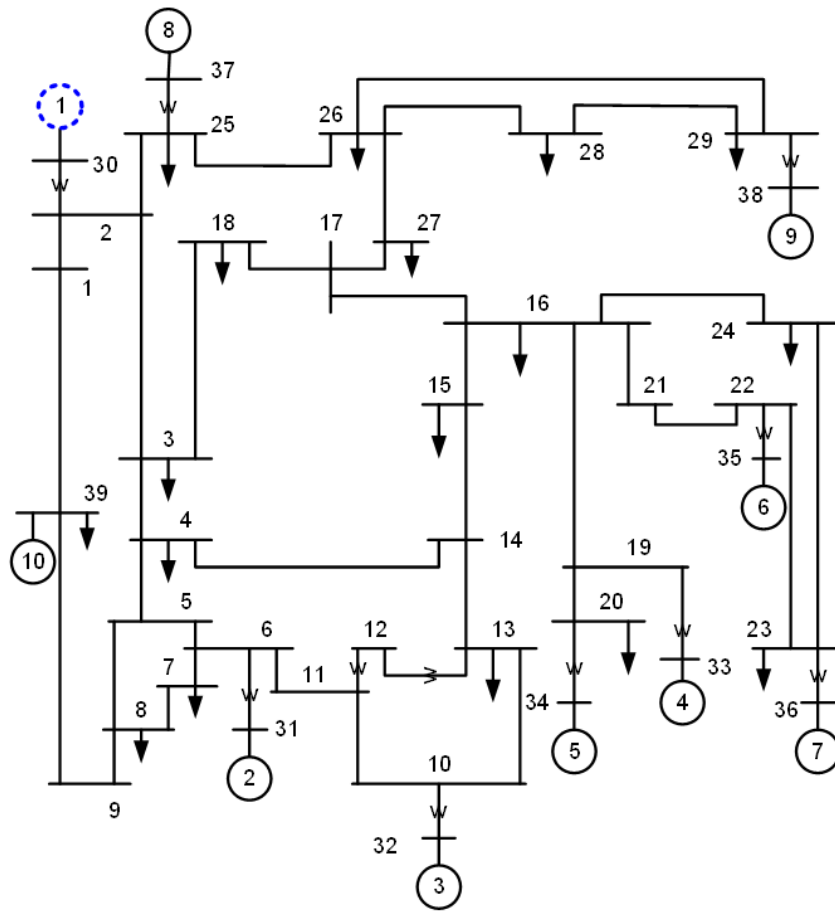


**Figure 20. IEEE 39-bus transmission test system**

## 5.3  Simulation Results

A generation outage at Bus 30 (marked in Figure 20) is created at 5 seconds. Figure 21 shows the frequency dynamic response of the system, and Figure 22 shows the DER AGC signals; both figures include various delay scenarios. One can observe that the 4-second delay causes system instability, and thus the delay margin is between 3 and 4 seconds in this setup ($k_P = 0.2$, $k_I = 0.2$). Note that in open networks, if multiple delays are included (e.g., communication/routing delay, congestion, latency, time needed for calculation), the total delay amount could be a few seconds or even longer [72], [73], [74]. This highlights the importance of considering delays when designing controllers, even more so with DERs and open communication networks.

The delay margins for different PI controller parameters, $k_P$ and $k_I$, are shown in Figure 23 as a 3D plot; the enclosed space between two surfaces is the feasible space of the three values ($k_P$, $k_I$, and delay), ensuring the stability of the system. Figure 24 also shows the feasible space but for conventional generators providing AGC scenarios. A comparison of the two figures shows that the upper and lower delay margins (surfaces) are quite different. In the DER case, when $k_P$, $k_I$ are large, shorter delays can cause system instability, whereas longer delays do not. This is because large values of $k_P$ and $k_I$ tend to overcompensate the system ACE, though the delays can offset this overcompensation to some degree; see the lower delay margin at $k_P = 0.3$, $k_I = 0.4$ in Figure 23. In the case of the conventional generators providing AGC, however, generally longer delays tend to have a higher risk of instability. This difference is because the response rate of the DERs (with inverters) is much faster than the traditional turbine governors. This demonstrates the different impacts of delays in AGC signals using DERs and traditional generation. Note that the simulated scenarios assume that all the delays are the same; scenarios with different delays will be included in future work.
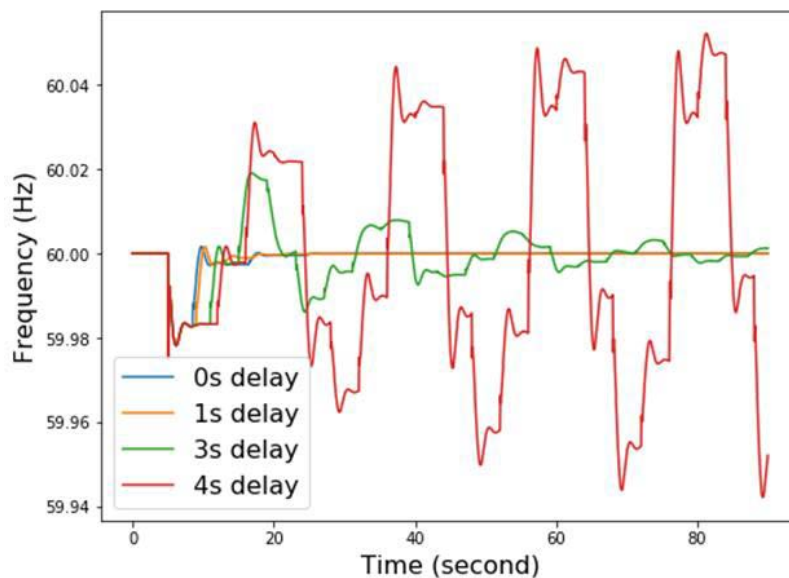


**Figure 21. System frequency response under different DER delay signals**
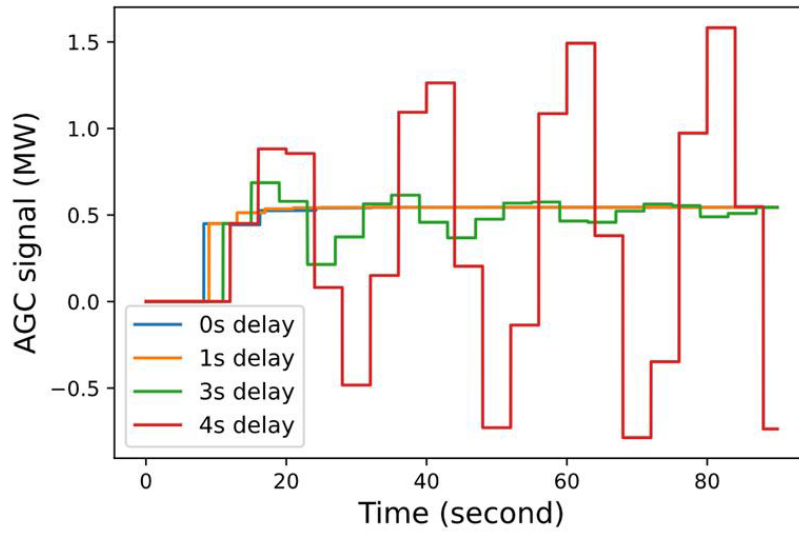
**Figure 22. DER AGC signals under different communication delays**
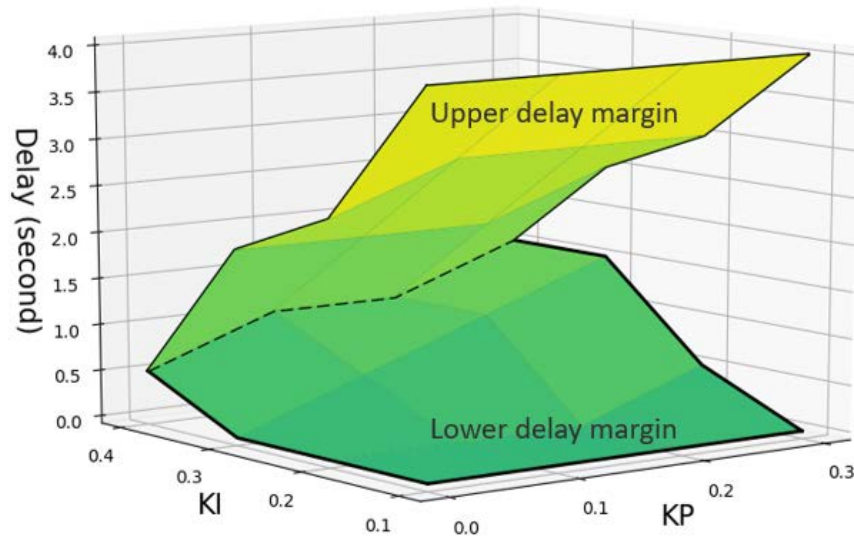


**Figure 23. Feasible space of the three values in DER AGC controls**
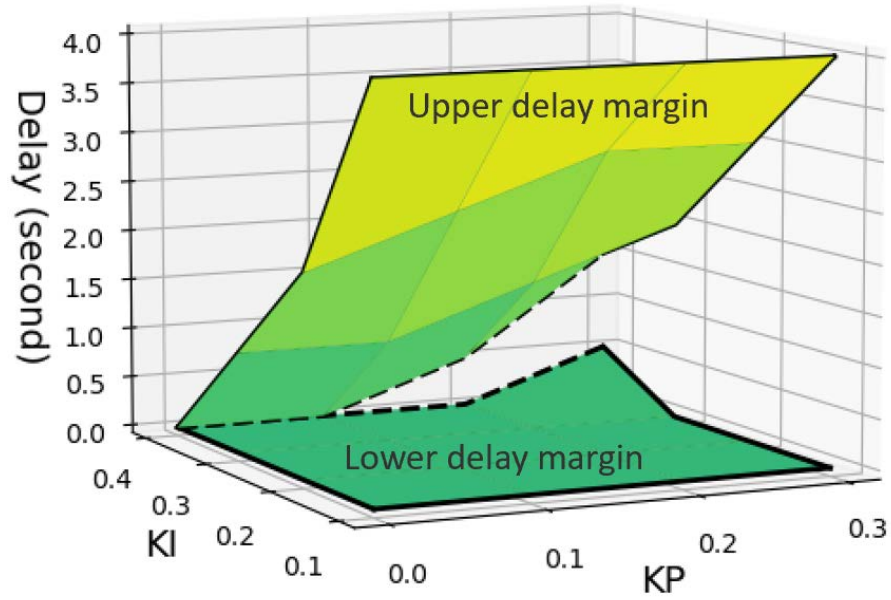
**Figure 24. Feasible space of the three values in turbine governor AGC controls**

# 6 Use Case 2: EVs Providing SFR

This section illustrates the EV smart charging impacts on frequency response by T&D co-simulation. Two sets of cases are studied. Case 1 explores the impacts of EVs providing frequency regulation on the system frequency response and EV charging profiles without communication variations. Case 2 studies the communication latency and packet loss of EV frequency regulation on the system frequency stability. Note that there is a difference between the unidirectional smart charging and the bidirectional vehicle-to-grid (V2G), which can involve discharging EV batteries. To accentuate the effect of communication variations, in this section, we consider V2G, but it is important to recognize that very similar results would apply for smart charging for twice the number of vehicles in terms of the same amount of power provided to the grid.

## 6.1 EV Dynamic Model

PEVs have promising capabilities to provide several T&D grid services [75]. Because EVs are essentially inverter-based resources, we developed an EV dynamic model based on the Western Electricity Coordinating Council PVD1 model [76]. Here, we added (1) a parameter, Pcap, that models the participation strategies of the EVs; and (2) the state-of-charge (SOC)-related blocks that decide the current flowing in and out of the battery, as shown in Figure 25. Note that a generic model of PFR is also included. The overall dynamic model can represent general EV battery behaviors, which is added to ANDES [36].
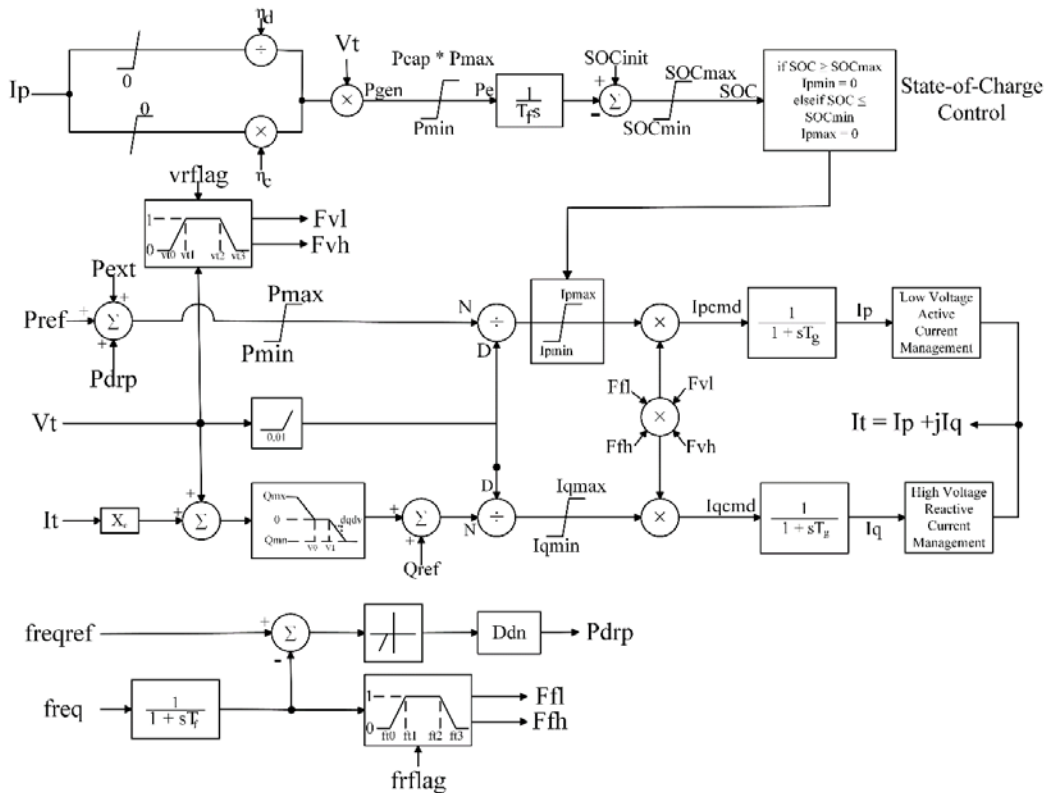


**Figure 25. Block diagram for EV dynamic model including PFR**

More specifically, Pcap added in this model limits the participation of an EV to provide frequency regulation. Pcap ranges from [-1, 1], and the meanings of the representative values are explained here. When Pcap = -1, the EV's maximum power is 100% charging, which means that the EV cannot provide PFR and SFR. When Pcap = 1, the EV's maximum power is 100% discharging, and the EV can change its status from charging to discharging to provide PFR and SFR. Similarly, Pcap = -0.5 and Pcap = 0.5 mean that the EV's maximum power is 50% charging and 50% discharging, respectively. Pcap = 0 represents that the EV's maximum power is 0, which means that the EV is not charging or discharging.

## 6.2 System Setup (Transmission-Distribution-Communication Systems)

The developed EV component enables EV frequency response studies. Now assume that the overall system comprises a transmission system, a control center, and an EV aggregator (have V2G capabilities) and a photovoltaic (PV) aggregator for each load bus, as shown in Figure 26. The transmission system sends the system frequency and the ACE signals to the transmission control center every 0.5 second, where the AGC signals are calculated with the PI controller and sent to the EV and PV aggregators every 4 seconds. This setup is modeled in HELICS, where the transmission simulation federate uses ANDES, and the distribution QSTS power flow uses OpenDSS.
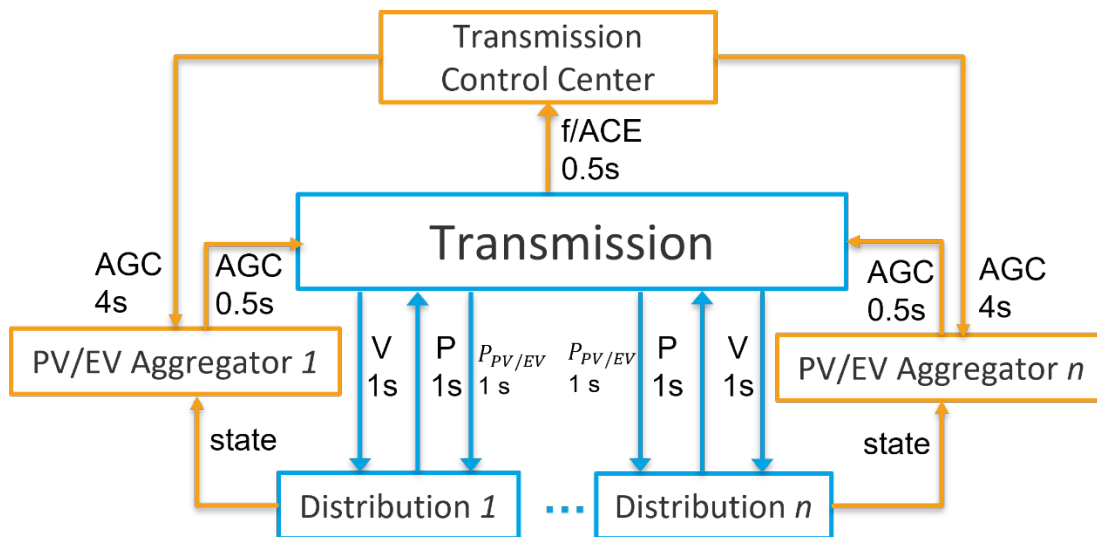


**Figure 26. Simulation components with information exchange for the transmission-distribution-communication system**

The same system is used for the transmission system shown in Figure 16. The transmission case can be found in [40], and the original data are in PSS/E format for the power flow (raw file) and dynamics (dyr file) data [60], [61]. Because some dynamic models in the original PSS/E data set are not supported by ANDES, a database conversion tool is developed. The unsupported dynamic models in the original case are converted to functionally similar and supported models in ANDES. The differences in the frequency profiles after selected N-1 contingency events stay below 10% compared to the original case. Conversion details are not discussed here because the purpose of this work is analyzing the V2G impact on frequency response rather than reproducing the original case. The power flow and dynamics data are parsed using a built-in tool in ANDES

and then fed into ANDES. The transmission network is tested in ANDES to ensure that the case can be properly initialized and has a flat start.

The distribution system covers the geographic area of Austin, Texas, and consists of six subregions [77]. The 243 distribution feeders in the five urban regions replace approximately 2.83 GW of load in the transmission system. A load total of 360,000 and more than 1 million electrical nodes are simulated in the distribution system. There are 8,400 DPV units and 42,000 EVs connected to distribution feeders (200 DPV units and 1,000 EVs at each of 36 substations and 400 DPV units and 2,000 EVs at each of the remaining 3 substations). Each EV is assumed to have a rated power of 7 kW [78] and a rated energy of 50 kWh. The assumed EV rated power of 7 kW is taken from [78]; most electric vehicles charging at home on a 240-V Level 2 charger will draw approximately 7,200 W or less. The total DPV power output is 222.7 MW, and the total installed DPV capacity is 2.1 GW, assuming a low PV power production time of the day, e.g., in the late afternoon. All 42,000 EVs consume 294 MW (charging at rated power) of power, and the total frequency regulation headroom is 588 MW (from rated charging to discharging). The co-simulation was performed on the HPC Eagle at NREL. The simulations assume that at 10 seconds, a generator in the Austin area, with 477 MW of real power output, is dropped. The SFR is provided only by the connected DPV and EVs in the system.

## 6.3  Simulation Scenarios without Communication Variations

This section illustrates the V2G impacts on frequency response by T&D co-simulation. Two sets of cases are studied. Case 1 explores the impact of the DPV and EVs on frequency response. Case 2 tests various EV participation strategies to analyze their effects on system frequency response.

### 6.3.1  Comparison between DPV and EV Frequency Regulation

This subsection explores the impacts of DPV and EVs on balancing generation and demand. Both PFR and SFR are considered. Details of each scenario are given in Table 3. In Case 1_1, the DPV and EVs do not provide SFR (AGC). In Case 1_2, only the DPV provides SFR; and it is the opposite in Case 1_3. In Case 1_4, both DPV and EVs provide SFR to the grid.

Table 3. Details of Four Scenarios

|  | Case 1_1 | Case 1_2 | Case 1_3 | Case 1_4 |
|---|---|---|---|---|
| DPV AGC | Off | On | Off | On |
| EV AGC | Off | Off | On | On |

Figure 27 shows the system frequency response after the generation trip event under the four cases. The system frequency drops immediately when the event happens, and it starts to recover soon afterward, with PFR from both conventional units and DERs (i.e., DPV and EVs). Without DERs providing SFR (Case 1_1), the system frequency cannot return to 60 Hz because in this testing system, conventional generators do not provide SFR. In both Case 1_2 and Case 1_3, the headroom of the DPV and EVs, respectively, are enough to cover the amount of generation loss, such that the frequency can be restored to 60 Hz after approximately 100 seconds. The frequency response curves of Case 1_2 and Case 1_3 are quite close because the dynamic parameters (droop parameters and inverter settings) of the EVs and DPV are the same. When both the DPV

36

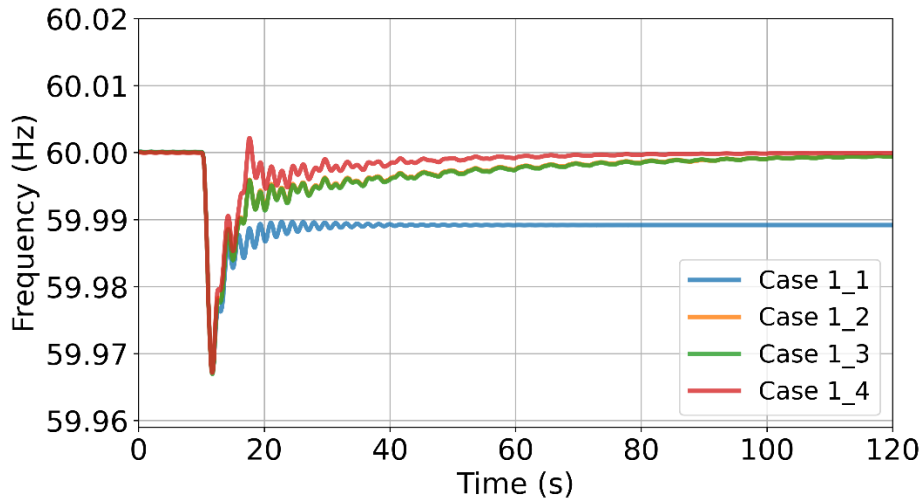and EVs provide SFR (Case 1_4), the system can recover, and the frequency recovery process is shorter.



**Figure 27. System frequency response under different scenarios**

Figure 28 demonstrates the impacts of the EV frequency regulation provision on its battery SOC. The EVs are constantly fully charging before the event. After the contingency, the PFR is activated first, and the SFR increases the power output of the EVs after receiving the AGC signal. As shown in the results from cases 1_1 and 1_2 (EV AGC off) and from cases 1_3 and 1_4 (EV AGC on), the EV charging patterns are all different despite the same EV AGC settings. The interactions between the system and the EVs change the charging speed of the EVs, as shown in the figure. More specifically, the EV charging speed is different in cases 1_1 and 1_2. In Case 1_1, because the system frequency cannot be restored to 60 Hz, the PFR of the EVs will be activated, and the EVs provide PFR to support the frequency during the whole simulation horizon; therefore, the EVs will not be fully charging in this case even when the frequency is stable, as shown in Figure 28. In Case 1_2, with the SFR support from the DPV, the system frequency can be restored to 60 Hz, and the PFR of the EVs will phase out once the frequency is restored; therefore, the power output of the EVs will be restored to fully charging once the frequency is restored to 60 Hz, as shown in Figure 29. In Case 1_3, the burden on the EVs is heavier (with only EVs providing SFR) compared with Case 1_4, when both the DPV and EVs provide SFR, so they start to discharge; therefore, the EVs start to discharge in Case 1_3. Consequently, the SOC of the EVs is the lowest in Case 1_3, when only the EVs provide SFR. The SOC of the EVs will be the highest in Case 1_2, when they do not provide SFR and the PFR reduces to 0. The EV power consumption varies as the EV and DPV frequency support strategies change. The SFR settings of both the EVs and DPV impact the charging pattern of the EVs.
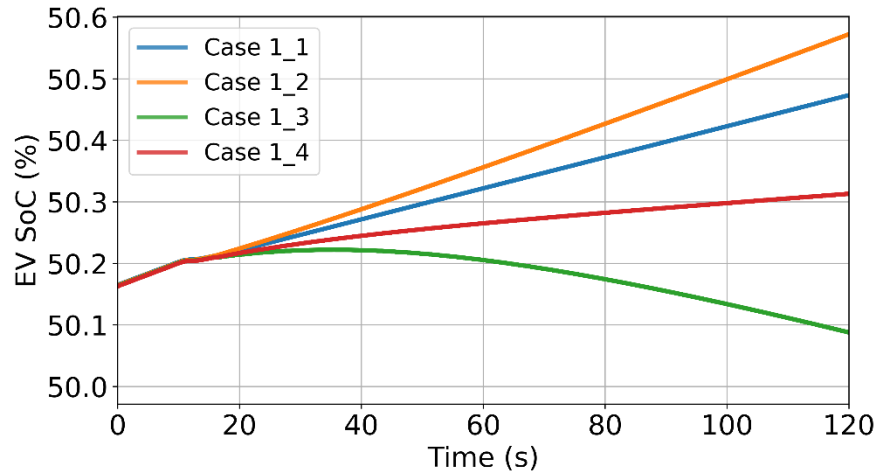
**Figure 28. EV SOC under different scenarios**
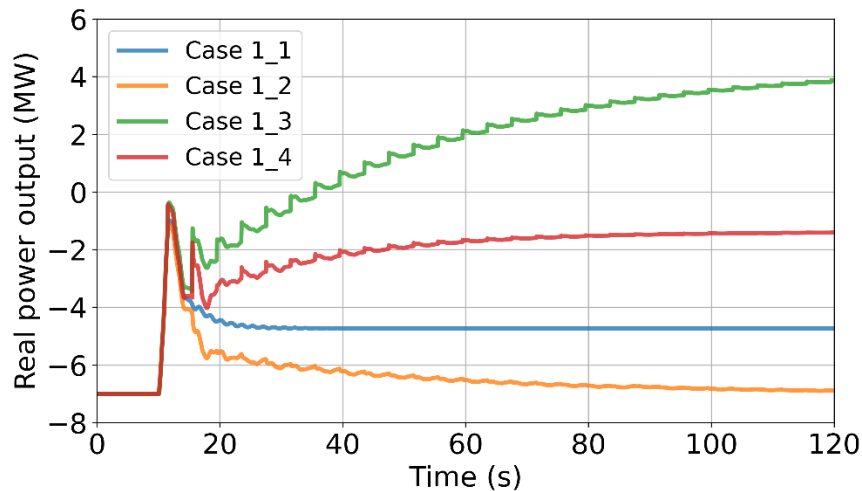


**Figure 29. EV real power output under different scenarios**

### 6.3.2 Impacts of EV Participation Factor

This subsection investigates the impacts of different EV frequency regulation strategies. Five EV frequency regulation strategies have been tested with varying Pcap values (i.e., -1, -0.5, 0, 0.5, 1), as discussed in Subsection II.A. The AGC signal is disabled for the DPV, so it does not provide any SFR.

When Pcap = -1 (the violet line in Figure 30 and Figure 31), the EVs do not have headroom for both PFR and SFR. The maximum power output of the EVs is 100% charging all the time. The EVs participate in neither PFR nor SFR. The EV charging rate is constant 100% all the time. Under this situation, the frequency nadir after the generation drop event is lower than Case 1_1 because the EVs cannot provide PFR with Pcap = -1, and the system frequency cannot return to 60 Hz. In Case 1_1, however, the EVs can still provide PFR without providing SFR.
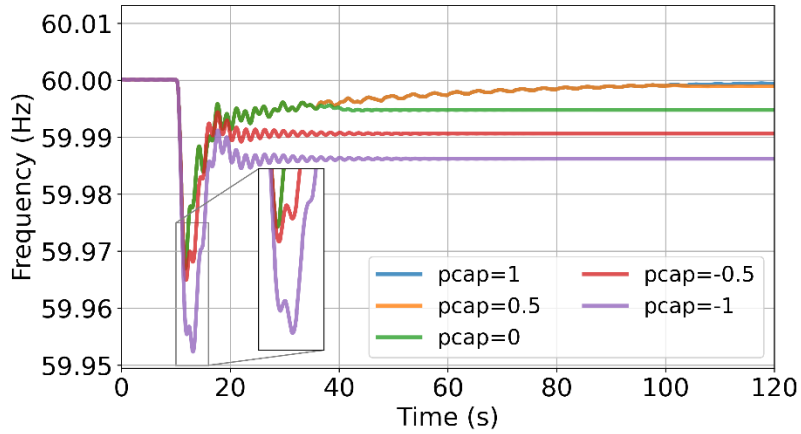
**Figure 30. Frequency response under five frequency regulation strategies**
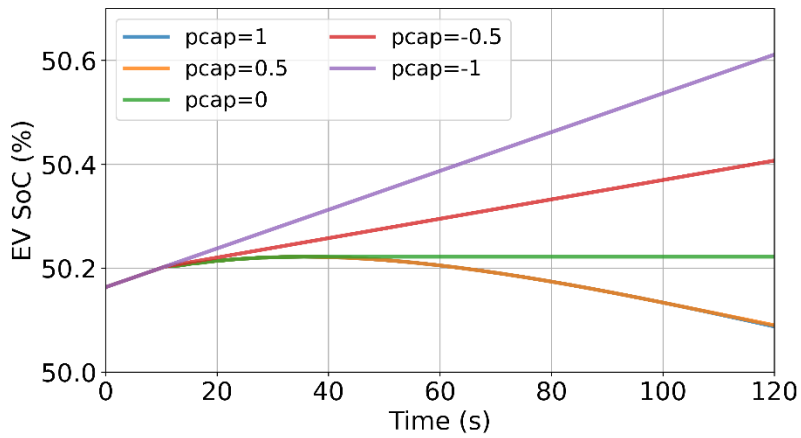


**Figure 31. EV SOC under five frequency regulation strategies**
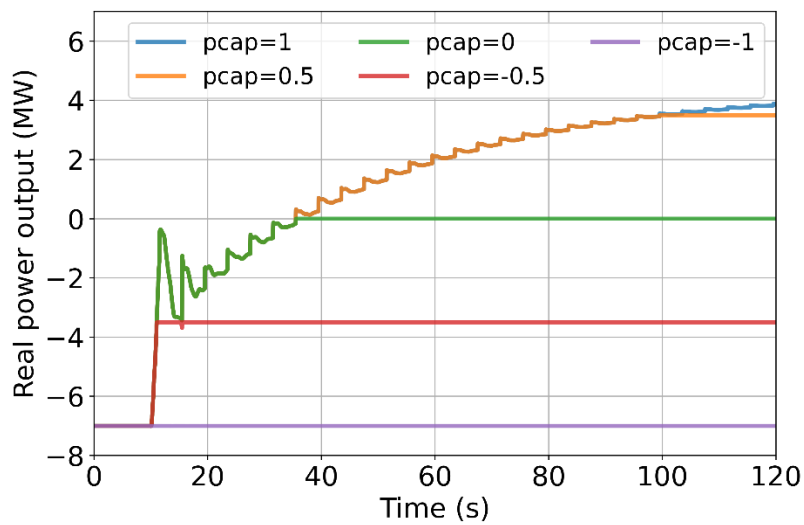


**Figure 32. EV power output under five frequency regulation strategies**

39

When Pcap = -0.5 (the red line), the maximum power output of the EVs is set to 50% charging. The frequency nadir is higher than that when Pcap = -1 because the EVs have 50% charging power headroom to provide PFR after the contingency with Pcap = -0.5. However, the nadir is lower than in the other scenarios because the PFR provided by the power headroom of the EVs is limited by the Pcap value; see Figure 32.

The scenario with Pcap = 0 (the green line) is an edge case. The charging rate of the EVs starts to decrease to 0 after the loss of generation. Starting from Pcap = 0, the amount of PFR power support is no longer limited by the EV headroom but by the droop parameters, and the frequency nadirs are almost the same because the droop parameters of the EVs are the same.

When Pcap > 0 (the blue and orange lines), the EVs can send power to the grid. After the contingency, the real power output increases (from charging to discharging), the SOC of the EVs decreases, and the system frequency gradually recovers. Note that there is only a slight difference when Pcap changes from 0.5 to 1 after 100 seconds for the three curves, including the system frequency response, the EV SOC, and the EV power output. This is because the total amount of power support from the PFR and SFR by the EVs with Pcap = 0.5 is nearly enough to cover the power imbalance.

Figure 33 shows the voltage profiles of a substation bus and all downstream feeder nodes. It shows the average voltage and the three-sigma (standard deviation) range of the voltage that covers 99% of the feeder's nodes. One can observe that the voltage increases and then decreases after the generation decreases because the local EVs/DPV participate in PFR and SFR. This demonstrates that the co-simulation model can capture the local voltage response.



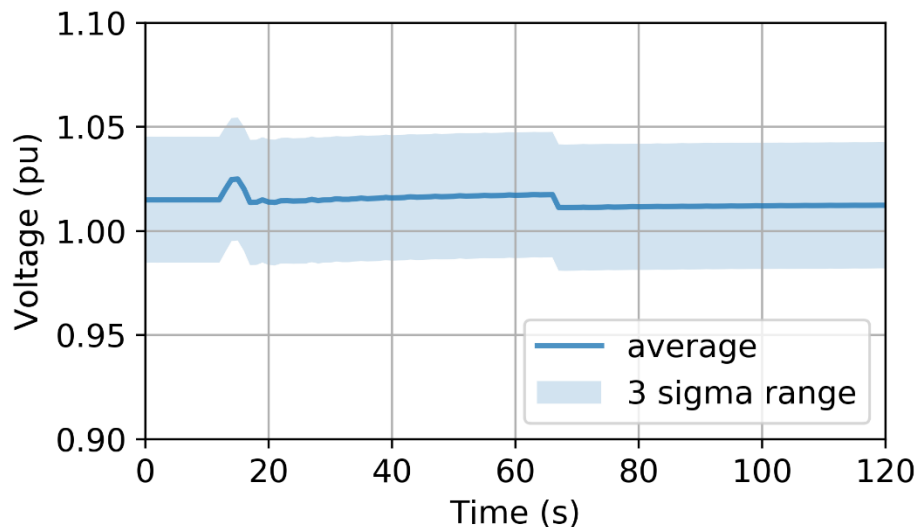**Figure 33. Case Pcap = 1, voltage of substation Bus 6032 with all downstream feeders, with medium-voltage and low-voltage nodes**

The simulation results demonstrate that the system conditions, the DER AGC settings, and the EV charging strategies all affect the system frequency response after contingencies. The proliferation of DERs, DPV, and EVs is crucial to the system frequency response, especially in future power systems.

## 6.4 Simulation Scenarios with Communication Variations

When using open communications, there are normally variations. This section illustrates the impacts of V2G with communication variations on the frequency response by T&D dynamic co-simulation. Two sets of cases are studied for the communication variations in the AGC signals: Case 1 explores the impact of the communication delay, and Case 2 tests the packet loss effects. The assumptions for the types of generation providing PFR and SFR are summarized in Table 4; the SFR is provided only by the connected EVs in the system. Each connected EV can provide support ranging from 100% charging to 100% discharging of rated power. The simulations assume that at 5 seconds, a generator in the Austin area, with 477 MW of real power output, is dropped.

**Table 4. Types of Generation**

| Generation Type | PFR | SFR |
|---|---|---|
| EV | Yes | Yes |
| DPV | Yes | No |
| Traditional unit | Yes | No |

### 6.4.1  Communication Layer Model and Settings in HELICS

Assume that the communication variations can happen each time whenever transmitting data are needed. In the developed framework, we add two filter functions in HELICS to each communication channel: a delay filter function and a packet loss filter function.

A delay filter function can keep a sending end point from sending the data until a preconfigured time is past and then pass on the data to the destination end point; this preconfigured time (read by a HELICS broker) can be a constant or generated randomly from a distribution, i.e., normal distribution. The normal distribution assumption is based on the information in [45]. This setup can model a constant or time-varying delay for different communication channels.

In addition, each transmit of data packet has a chance of losing the packet (e.g., caused by hardware failure), resulting in the data packet either successfully passing or failing to pass. These events are naturally modeled as Bernoulli distributions and are parameterized by a single variable, p, the probability of packet loss, with p in [0,1]. Inside HELICS, the added packet loss filter function can remove the packet data probabilistically and not send it to the destination end point. Note that we allow different values of p for different communication channels.

### 6.4.2  Impact of Homogeneous and Heterogeneous Delays

#### 6.4.2.1  Homogeneous

Figure 34 shows the homogeneous delay with different delay times: i.e., 0, 2, 4, 10, and 20 seconds. It shows that longer delay times result in longer system frequency recovery. It is straightforward that with a large delay, the system needs a long time to restore frequency to the nominal value.

41
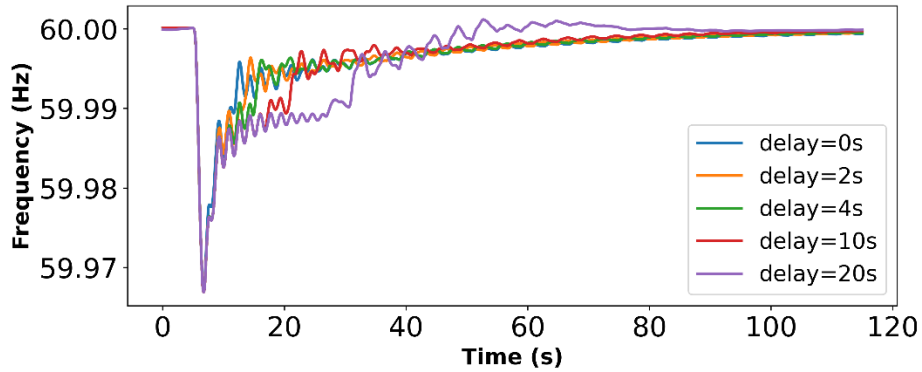
**Figure 34. Homogeneous delay with different delay times**

Figure 35 shows an EV power output change from charging (negative value) to discharging (positive value) for the SFR. This figure also shows that when there is a communication delay, the PEV SFR will respond with a delay. Further, the longer the delay time, the later the SFR will respond. Accordingly, this will result in a change in its SOC, as shown in Figure 36. When a PEV is providing frequency regulation, its SOC can change from increasing to decreasing, which might slightly increase the PEV's charging time. Despite its insignificant impact, this should still be considered by PEV owners when a PEV is enabled to provide frequency regulation. Figure 37 shows one distribution feeder voltage as an example to demonstrate the capability of the framework in also capturing the system impact at the distribution side. In this case, the impacts of the communication delay on the distribution feeder's voltage profile are insignificant and might be trivial.

42
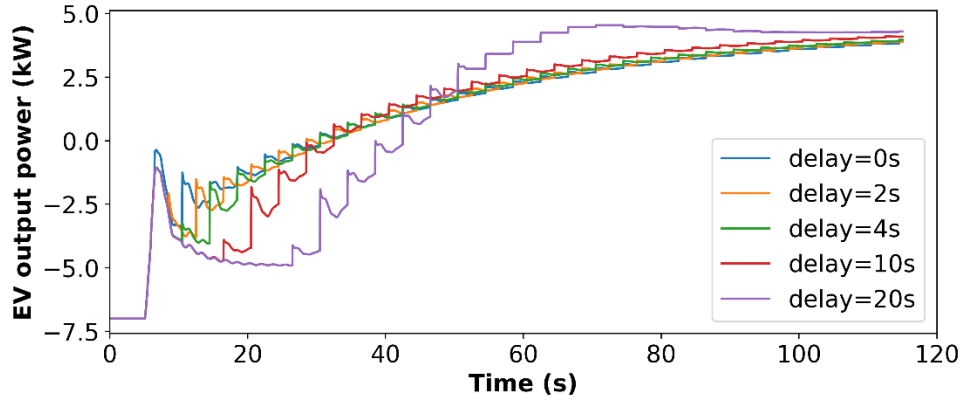
**Figure 35. EV power output example**
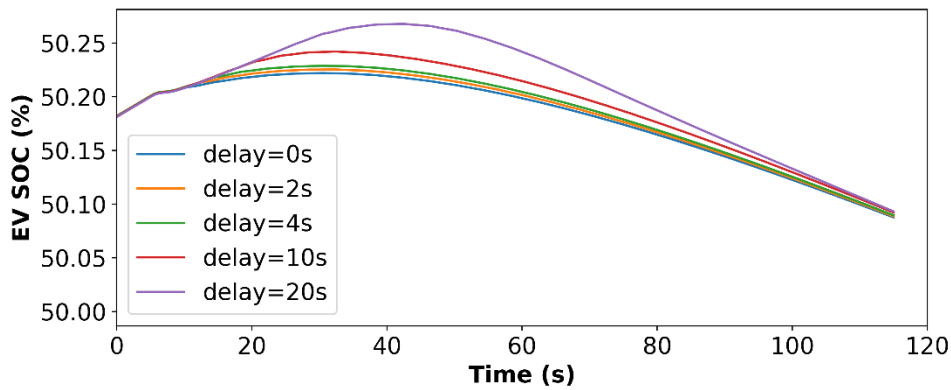


**Figure 36. EV SOC example**
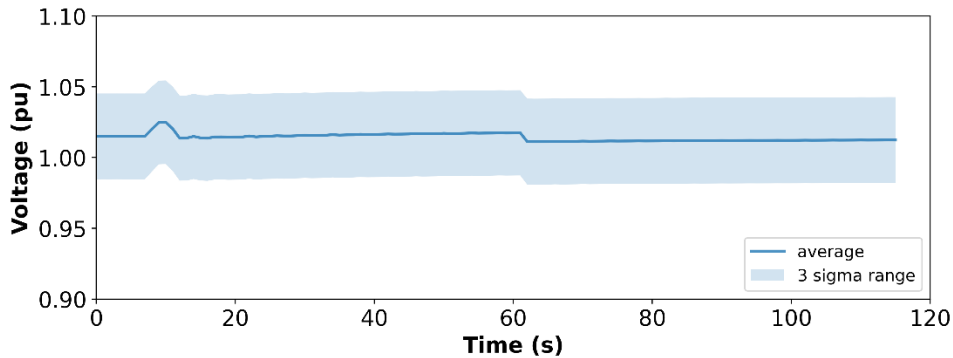


**Figure 37. Distribution bus voltage example: the average and 3-sigma range of the voltages among all medium-voltage nodes**

### 6.4.2.2 Heterogeneous

To simulate the time-varying and heterogeneous delay cases (i.e., different channels of AGC signal have different delays), it is assumed that each EV channel transmitting data each time has a delay time that follows a normal distribution, i.e., $T_{delay} \sim N(\mu, \sigma^2)$ with mean, μ, and standard deviation, σ. Figure 38 shows the comparison of the system frequency response under different normally distributed delay time assumptions. It shows that the impacts of the standard deviation of the delay time are not as significant as its mean value. This is because the control

43

signals affected by the dispersed delay times (random delay times deviate from the mean) compensate each other; thus, compared to the standard deviation of the communication delay, the mean values of the communication delay have a more noticeable impact on the system frequency recovery.
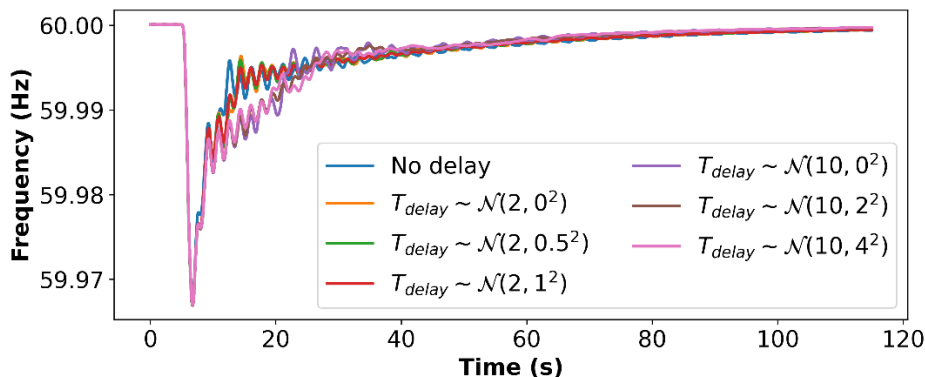


**Figure 38. Heterogeneous delay with different delay times**

### 6.4.3 *Impact of Homogeneous and Heterogeneous Packet Loss*

Packet loss occurs when one or more packets of data traveling across a communication network fail to reach their destination. Packet loss is caused by either errors in data transmission, typically across wireless networks, or network congestion. Packet loss measures whether a packet sent is successful or fails each time, i.e., $X \sim \text{Bernoulli}(p_{\text{loss}})$, where $X \in \{0,1\}$, and the loss rate $p_{loss} \in [0,1]$. For example, if a transmission channel has a loss rate of 0.2, it means that there is a 20% chance the transmitting packet is lost each time the transmission channel is used.

#### 6.4.3.1 Homogeneous

Figure 39 shows the comparison of the homogeneous packet loss with different loss rates. It shows that the packet drop impacts are not as significant as the communication delays. This is because the packet drop is random, and the packet drops of different channels can offset the impacts of each other.
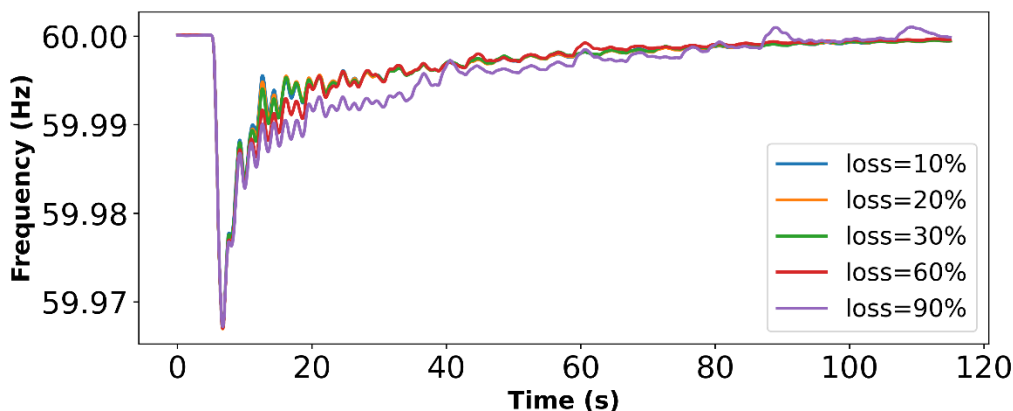


**Figure 39. Homogeneous packet loss with different loss rates**

44

### 6.4.3.2 Heterogeneous

The loss rates of different communication channels can be different and are assumed to be different this time. To represent the diversity of the loss rates, they are generated randomly for each communication channel from a normal distribution, i.e., $P_{loss} \sim N(\mu, \sigma^2)$ with mean, $\mu$, and standard deviation, $\sigma$. The simulated cases in Figure 40 do not show significant different impacts on the system frequency recovery times. It is also observed that compared to the homogeneous packet drop in Figure 40, the heterogeneous packet drop has a smaller impact on the system frequency recovery. This can be explained by the random packet drop compensating the effects of each other.
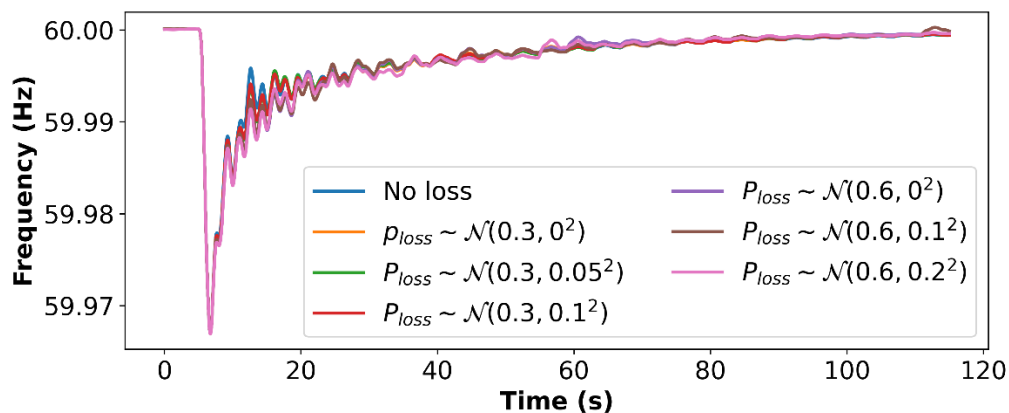


**Figure 40. Heterogeneous loss with different loss rates**

All the simulation results demonstrate the impact of the communication variations on the LFC by EVs using publicly available, open communication networks. The results show that as the delay and packet loss rates increase, the system frequency tends to recover more slowly. In extreme cases, the system frequency might oscillate (e.g., 20-second delay case). The heterogeneous cases show a smooth effect in the AGC [51]. In addition, the deviations of the communication variations among different channels are less significant compared with the mean values.

# 7 Conclusions

DERs, including DPV and PEV, have been increasingly deployed in power systems. To leverage their PFR and SFR services to stabilize the system frequency, their dynamic responses in T&D networks should be accurately and efficiently modeled. This report demonstrates an efficient, open-source T&D dynamic co-simulation methodology framework to model the frequency dynamic responses of DERs providing PFR and SFR considering their communication latencies and packet losses. Their impacts on both the transmission system frequency response and the distribution feeder voltage are modeled. The analyzed scenarios include normal load variations and contingencies such as generation outages. The results show that DERs can provide reliable PFR and SFR to stabilize the system frequency given certain headroom considering local voltage constraints.

The co-simulations of the transmission-distribution-communication systems bridge the gap of the missing interactive considerations among simulators while simultaneously considering the performance simulations of each system. For example, (1) DPV power intermittency regarding the maximum available power and the maximum limits enforced by local distribution feeders can be endogenously considered in the proposed co-simulation model; therefore, real-time PFR and SFR delivery can be guaranteed to maintain transmission system frequency stability and distribution system voltage profiles; and (2) PEV charging strategies that should be decided by PEV owners can also be considered in the co-simulation.

The first use case demonstration explores the impacts of the delayed DER AGC signals on the frequency stability of the system. The simulation results with hundreds of DERs show that the risk of system instability might substantially increase if the design of the DER AGC control fails to consider communication variations. The communication delay margin of DER AGC can be quite different from that of conventional generators; therefore, system operators should consider communication delays when designing DER AGC control parameters and when dispatching DERs for AGC services.

The second use case studies the impacts of EVs on the system frequency regulation with and without communication variations. Simulations without communication variations demonstrate that the aggregation of EVs has great potential to provide both PFR and SFR to quickly restore the system frequency after contingencies. Several factors impact EV frequency regulation, such as the participation factor and the potential SOC limits. When EVs are enabled to change their status from fully charging to fully discharging, their capability and flexibility to provide frequency regulation are the largest, and the system frequency can be restored the fastest. Although the results presented in this report are based on several assumptions, the outcomes can still reveal the EV impact on frequency response using the T&D co-simulation platform. EV frequency regulation with communication variations demonstrate that the mean values of the communication delay have a higher impact on the frequency recovery than the standard deviation of the delay. Meanwhile, the packet drop impacts on the frequency restoration are not significant in both the homogeneous and heterogeneous packet drop rates. In addition, different from the traditional analytical method (i.e., state-space equations), the co-simulation method can observe different aspects of the impacts, e.g., heterogeneous communication impacts and local grid constraints, such as voltage and reverse power flow.

In summary, the developed CPDS framework is scalable and can greatly improve the utilization of DERs to provide grid services. The quantitative analysis and modeling scheme in this report can provide insights into designing future LFC algorithms and communication planning for LFC with DERs such as DPV and PEVs.

Future work includes modeling all the reliability services as well as modeling more comprehensive transients and dynamic behaviors regarding DER power electronic devices and their control strategies, research on the robust controls of DERs against communication variations and on communication requirements for grid services under publicly available networks and theoretical analysis regarding the stability of the discrete AGC signal of DERs. Future work will also include research on the coordination between EV charging scheduling and frequency regulation to maintain a better trade-off of the system frequency stability and the EV charging time.

# References

[1] Y. Chen, R. Leonard, M. Keyser, and J. Gardner, "Development of performance-based two-part regulating reserve compensation on miso energy and ancillary service market," *IEEE Trans. Power Syst.*, vol. 30, no. 1, pp. 142–155, 2015, doi: 10.1109/TPWRS.2014.2320519.

[2] "NERC | Distributed Energy Resources Connection Modeling and Reliability Considerations," 2017.

[3] B. Zhang, A. Y. S. Lam, A. D. Dominguez-Garcia, and D. Tse, "An Optimal and Distributed Method for Voltage Regulation in Power Distribution Systems," *IEEE Trans. Power Syst.*, vol. 30, no. 4, pp. 1714–1726, 2015, doi: 10.1109/TPWRS.2014.2347281.

[4] X. Zhou, Z. Liu, C. Zhao, and L. Chen, "Accelerated Voltage Regulation in Multi-Phase Distribution Networks Based on Hierarchical Distributed Algorithm," *IEEE Trans. Power Syst.*, pp. 1–1, Oct. 2019, doi: 10.1109/tpwrs.2019.2948978.

[5] X. Zhou, Z. Liu, W. Wang, C. Zhao, F. Ding, and L. Chen, "Hierarchical distributed voltage regulation in networked autonomous grids," in *Proceedings of the American Control Conference*, 2019, vol. 2019-July, pp. 5563–5569, doi: 10.23919/acc.2019.8814670.

[6] Z. Yi, Y. Xu, W. Gu, and Z. Fei, "Distributed Model Predictive Control Based Secondary Frequency Regulation for a Microgrid with Massive Distributed Resources," *IEEE Trans. Sustain. Energy*, pp. 1–1, 2020, doi: 10.1109/TSTE.2020.3033320.

[7] M. Bayat, K. Sheshyekani, M. Hamzeh, and A. Rezazadeh, "Coordination of Distributed Energy Resources and Demand Response for Voltage and Frequency Support of MV Microgrids," *IEEE Trans. Power Syst.*, vol. PP, no. 99, pp. 1–11, 2015, doi: 10.1109/TPWRS.2015.2434938.

[8] Q. Shi, F. Li, G. Liu, D. Shi, Z. Yi, and Z. Wang, "Thermostatic Load Control for System Frequency Regulation Considering Daily Demand Profile and Progressive Recovery," *IEEE Trans. Smart Grid*, vol. 10, no. 6, pp. 6259–6270, Nov. 2019, doi: 10.1109/TSG.2019.2900724.

[9] X. Fang, H. Yuan, and J. Tan, "Secondary Frequency Regulation from Variable Generation through Uncertainty Decomposition: An Economic and Reliability Perspective," *IEEE Trans. Sustain. Energy*, pp. 1–1, 2021, doi: 10.1109/TSTE.2021.3076758.

[10] C. Cano, "FERC Order No. 2222: A New Day for Distributed Energy Resources," 2020.

[11] "PSLF | Transmission Planning Software | GE Energy Consulting." .

[12] "PSS®E – transmission planning and analysis | PSS® power system simulation and modeling software | Siemens Global." .

[13] "PowerWorld » The visual approach to electric power systems." .

[14] "Reliability Guideline: Parameterization of the DER_A Model." .

[15] G. Krishnamoorthy and A. Dubey, "Transmission–Distribution Cosimulation: Analytical Methods for Iterative Coupling," *IEEE Syst. J.*, vol. 14, no. 2, pp. 2633–2642, Jun. 2020,

doi: 10.1109/JSYST.2019.2931201.

[16] R. Sadnan, G. Krishnamoorthy, and A. Dubey, "Transmission and Distribution (TD) Quasi-Static Co-Simulation: Analysis and Comparison of TD Coupling Strength," *IEEE Access*, vol. 8, pp. 124007–124019, 2020, doi: 10.1109/ACCESS.2020.3006058.

[17] Z. Li, Q. Guo, H. Sun, and J. Wang, "Coordinated transmission and distribution AC optimal power flow," *IEEE Trans. Smart Grid*, vol. 9, no. 2, pp. 1228–1240, 2018, doi: 10.1109/TSG.2016.2582221.

[18] S. M. Mohseni-Bonab, A. Hajebrahimi, I. Kamwa, and A. Moeini, "Transmission and distribution co-simulation: A review and propositions," *IET Generation, Transmission and Distribution*, vol. 14, no. 21. Institution of Engineering and Technology, pp. 4631–4642, Nov. 2020, doi: 10.1049/iet-gtd.2020.0244.

[19] B. Palmintier *et al.*, "IGMS: An Integrated ISO-To-Appliance Scale Grid Modeling System," *IEEE Trans. Smart Grid*, vol. 8, no. 3, pp. 1525–1534, May 2017, doi: 10.1109/TSG.2016.2604239.

[20] A. Hariri and M. O. Faruque, "Impacts of distributed generation on power quality," Nov. 2014, doi: 10.1109/NAPS.2014.6965404.

[21] X. Zhang, R. Dai, P. Wei, Y. Liu, G. Liu, and Z. Wang, "Power System Transient Modeling and Simulation using Integrated Circuit," Jun. 2021.

[22] Y. Liu, X. Zhang, R. Dai, and G. Liu, "Using Terminal Circuit for Power System Electromagnetic Transient Simulation," Jul. 2021.

[23] Q. Huang and V. Vittal, "Advanced EMT and phasor-domain hybrid simulation with simulation mode switching capability for transmission and distribution systems," *IEEE Trans. Power Syst.*, vol. 33, no. 6, pp. 6298–6308, Nov. 2018, doi: 10.1109/TPWRS.2018.2834561.

[24] Q. Huang and V. Vittal, "Integrated Transmission and Distribution System Power Flow and Dynamic Simulation Using Mixed Three-Sequence/Three-Phase Modeling," *IEEE Trans. Power Syst.*, vol. 32, no. 5, pp. 3704–3714, Sep. 2017, doi: 10.1109/TPWRS.2016.2638910.

[25] H. Jain, A. Parchure, R. P. Broadwater, M. Dilek, and J. Woyak, "Three-Phase Dynamic Simulation of Power Systems Using Combined Transmission and Distribution System Models," *IEEE Trans. Power Syst.*, vol. 31, no. 6, pp. 4517–4524, Nov. 2016, doi: 10.1109/TPWRS.2016.2535297.

[26] M. A. Elizondo, F. K. Tuffner, and K. P. Schneider, "Three-Phase Unbalanced Transient Dynamics and Powerflow for Modeling Distribution Systems With Synchronous Machines," *IEEE Trans. Power Syst.*, vol. 31, no. 1, pp. 105–115, Jan. 2016, doi: 10.1109/TPWRS.2015.2389712.

[27] A. Hariri and M. O. Faruque, "A Hybrid Simulation Tool for the Study of PV Integration Impacts on Distribution Networks," *IEEE Trans. Sustain. Energy*, vol. 8, no. 2, pp. 648–657, Apr. 2017, doi: 10.1109/TSTE.2016.2614960.

[28] "OpenDSS / Code / [r2960] /trunk/Distrib/Doc/OpenDSSManual.pdf." .

[29]    R. Huang, R. Fan, J. Daily, A. Fisher, and J. Fuller, "Open-source framework for power system transmission and distribution dynamics co-simulation," *IET Gener. Transm. Distrib.*, vol. 11, no. 12, pp. 3152–3162, Aug. 2017, doi: 10.1049/iet-gtd.2016.1556.

[30]    R. Venkatraman, S. K. Khaitan, and V. Ajjarapu, "Dynamic Co-Simulation Methods for Combined Transmission-Distribution System with Integration Time Step Impact on Convergence," *IEEE Trans. Power Syst.*, vol. 34, no. 2, pp. 1171–1181, Mar. 2019, doi: 10.1109/TPWRS.2018.2874807.

[31]    R. W. Kenyon, B. Mather, and B. M. Hodge, "Coupled transmission and distribution simulations to assess distributed generation response to power system faults," *Electr. Power Syst. Res.*, vol. 189, p. 106746, Dec. 2020, doi: 10.1016/j.epsr.2020.106746.

[32]    P. Kundur, *Power System Stability and Control*. New York: McGraw-Hill, 1994.

[33]    K. Tomsovic, D. E. Bakken, V. Venkatasubramanian, and A. Bose, "Designing the next generation of real-time control, communication, and computations for large power systems," in *Proceedings of the IEEE*, 2005, vol. 93, no. 5, pp. 965–979, doi: 10.1109/JPROC.2005.847249.

[34]    F. Zhang, Y. Sun, L. Cheng, X. Li, J. H. Chow, and W. Zhao, "Measurement and Modeling of Delays in Wide-Area Closed-Loop Control Systems," *IEEE Trans. Power Syst.*, vol. 30, no. 5, pp. 2426–2433, Sep. 2015, doi: 10.1109/TPWRS.2014.2359773.

[35]    H. Ye, K. Liu, Q. Mou, and Y. Liu, "Modeling and formulation of delayed cyber-physical power system for small-signal stability analysis and control," *IEEE Trans. Power Syst.*, vol. 34, no. 3, pp. 2419–2432, May 2019, doi: 10.1109/TPWRS.2018.2890540.

[36]    H. Cui, F. Li, and K. Tomsovic, "Hybrid Symbolic-Numeric Framework for Power System Modeling and Analysis," *IEEE Trans. Power Syst.*, pp. 1–1, Feb. 2020, doi: 10.1109/TPWRS.2020.3017019.

[37]    B. Palmintier, D. Krishnamurthy, P. Top, S. Smith, J. Daily, and J. Fuller, "Design of the HELICS high-performance transmission-distribution-communication-market go-simulation framework," Oct. 2017, doi: 10.1109/MSCPES.2017.8064542.

[38]    "HELICS." https://helics.org/ (accessed Apr. 13, 2021).

[39]    J. Zhang *et al.*, "Development of HELICS-based high-performance cyber-physical co-simulation framework for distributed energy resources applications," Nov. 2020, doi: 10.1109/SmartGridComm47815.2020.9302977.

[40]    "Electric Grid Test Case Repository." .

[41]    W. Wang, X. Fang, H. Cui, F. Li, Y. Liu, and T. J. Overbye, "Transmission-and-Distribution Dynamic Co-simulation Framework for Distributed Energy Resource Frequency Response," *IEEE Trans. Smart Grid*, 2021, doi: 10.1109/TSG.2021.3118292.

[42]    W. Wang, X. Fang, and A. Florita, "Impact of DER Communication Delay in AGC: Cyber-Physical Dynamic Co-simulation," *2021 IEEE 48th Photovolt. Spec. Conf.*, pp. 2616–2620, Jun. 2021, doi: 10.1109/PVSC43889.2021.9518779.

[43]    Y. Liu *et al.*, "Transmission-Distribution Dynamic Co-simulation of Electric Vehicles Providing Grid Frequency Response," 2022.

[44] J. M. T. Marinho and G. N. Taranto, "A hybrid three-phase single-phase power flow formulation," *IEEE Trans. Power Syst.*, vol. 23, no. 3, pp. 1063–1070, 2008, doi: 10.1109/TPWRS.2008.922567.

[45] A. Khalil, J.-H. Wang, and O. Mohamed, "Robust Stabilization of Load Frequency Control System Under Networked Environment," *Int. J. Autom. Comput.*, vol. 14, no. 1, pp. 93–105, 2017, doi: 10.1007/s11633-016-1041-z.

[46] C. R. -, "Report:  2002-12-10  Vehicle to Grid Demonstration Project: Grid Regulation Ancillary Service with a Battery Electric Vehicle," 2002, Accessed: Mar. 28, 2022. [Online]. Available: www.acpropulsion.com.

[47] W. Kempton, "Vehicle to Grid Demonstration Project," Newark, DE, 2010. Accessed: Mar. 28, 2022. [Online]. Available: https://www.osti.gov/servlets/purl/1053603.

[48] D. T. Hoang, P. Wang, D. Niyato, and E. Hossain, "Charging and discharging of plug-in electric vehicles (PEVs) in vehicle-to-grid (V2G) systems: A cyber insurance-based model," *IEEE Access*, vol. 5, pp. 732–754, 2017, doi: 10.1109/ACCESS.2017.2649042.

[49] "WECC Distributed and Small PV Plants Generic Model (PVD1) - ESIG." .

[50] NERC, "Special Report: Ancillary Service and Balancing Authority Area Solutions to Integrate Variable Generation," 2011.

[51] T. J. Overbye, K. S. Shetye, J. Wert, H. Li, C. Cathey, and H. Scribner, "Stability Considerations for a Synchronous Interconnection of the North American Eastern and Western Electric Grids," Accessed: Apr. 06, 2022. [Online]. Available: https://hdl.handle.net/10125/79776.

[52] X. Fang, B.-M. S. Hodge, E. Du, C. Kang, and F. F. Li, "Introducing Uncertainty Components in Locational Marginal Prices for Pricing Wind Power and Load Uncertainties," *IEEE Trans. Power Syst.*, vol. 34, no. 3, pp. 2013–2024, 2019, doi: 10.1109/TPWRS.2018.2881131.

[53] X. Fang, H. Cui, E. Du, F. Li, and C. Kang, "Characteristics of locational uncertainty marginal price for correlated uncertainties of variable renewable generation and demands," *Appl. Energy*, vol. 282, p. 116064, Jan. 2021, doi: 10.1016/j.apenergy.2020.116064.

[54] X. Fang, K. S. A. Sedzro, H. Yuan, H. Ye, and B.-M. Hodge, "Deliverable Flexible Ramping Products Considering Spatiotemporal Correlation of Wind Generation and Demand Uncertainties," *IEEE Trans. Power Syst.*, vol. 35, no. 4, pp. 2561–2574, Dec. 2020, doi: 10.1109/TPWRS.2019.2958531.

[55] X. Fang, B. M. Hodge, H. Jiang, and Y. Zhang, "Decentralized wind uncertainty management: Alternating direction method of multipliers based distributionally-robust chance constrained optimal power flow," *Appl. Energy*, vol. 239, no. 2019, pp. 938–947, Apr. 2019, doi: 10.1016/j.apenergy.2019.01.259.

[56] H. Cui and F. Li, "ANDES: A Python-Based Cyber-Physical Power System Simulation Tool," Jan. 2019, doi: 10.1109/NAPS.2018.8600596.

[57] H. Cui, F. Li, J. H. Chow, and L. Fellow, "Mass-Matrix Differential-Algebraic Equation Formulation for Transient Stability Simulation."

[58]  "Tutorial — ANDES 1.3.0 documentation." .

[59]  X. Zhu, J. Wang, N. Lu, N. Samaan, R. Huang, and X. Ke, "A Hierarchical VLSM-Based Demand Response Strategy for Coordinative Voltage Control between Transmission and Distribution Systems," *IEEE Trans. Smart Grid*, Sep. 2018, doi: 10.1109/TSG.2018.2869367.

[60]  A. B. Birchfield, T. Xu, K. M. Gegner, K. S. Shetye, and T. J. Overbye, "Grid Structural Characteristics as Validation Criteria for Synthetic Networks," *IEEE Trans. Power Syst.*, vol. 32, no. 4, pp. 3258–3265, Jul. 2017, doi: 10.1109/TPWRS.2016.2616385.

[61]  T. Xu, A. B. Birchfield, and T. J. Overbye, "Modeling, tuning, and validating system dynamics in synthetic electric grids," *IEEE Trans. Power Syst.*, vol. 33, no. 6, pp. 6501–6509, Nov. 2018, doi: 10.1109/TPWRS.2018.2823702.

[62]  H. Li *et al.*, "Building Highly Detailed Synthetic Electric Grid Data Sets for Combined Transmission and Distribution Systems," *IEEE Open Access J. Power Energy*, vol. 7, pp. 478–488, 2020, doi: 10.1109/OAJPE.2020.3029278.

[63]  "Eagle Computing System | High-Performance Computing | NREL." .

[64]  K. P. Schneider *et al.*, "Analytic Considerations and Design Basis for the IEEE Distribution Test Feeders," *IEEE Trans. Power Syst.*, vol. 33, no. 3, pp. 3181–3188, May 2018, doi: 10.1109/TPWRS.2017.2760011.

[65]  N. Panossian, T. Elgindy, B. Palmintier, and D. Wallison, "Synthetic, Realistic Transmission and Distribution Co-Simulation for Voltage Control Benchmarking," *2021 IEEE Texas Power Energy Conf. TPEC 2021*, Feb. 2021, doi: 10.1109/TPEC51183.2021.9384935.

[66]  Chuan-ke Zhang, Lin Jiang, Q. H. Wu, Yong He, and Min Wu, "Delay-dependent robust load frequency control for time delay power systems," Dec. 2013, pp. 1–1, doi: 10.1109/pesmg.2013.6672681.

[67]  X. Yu and K. Tomsovic, "Application of linear matrix inequalities for load frequency control with communication delays," *IEEE Trans. Power Syst.*, vol. 19, no. 3, pp. 1508–1515, Aug. 2004, doi: 10.1109/TPWRS.2004.831670.

[68]  L. Jiang, W. Yao, Q. H. Wu, J. Y. Wen, and S. J. Cheng, "Delay-dependent stability for load frequency control with constant and time-varying delays," *IEEE Trans. Power Syst.*, vol. 27, no. 2, pp. 932–941, May 2012, doi: 10.1109/TPWRS.2011.2172821.

[69]  H. Luo, I. A. Hiskens, and Z. Hu, "Stability Analysis of Load Frequency Control Systems with Sampling and Transmission Delay," *IEEE Trans. Power Syst.*, vol. 35, no. 5, pp. 3603–3615, Sep. 2020, doi: 10.1109/TPWRS.2020.2980883.

[70]  T. Kerci, M. A. A. Murad, I. Dassios, and F. Milano, "On the Impact of Discrete Secondary Controllers on Power System Dynamics," *IEEE Trans. Power Syst.*, 2021, doi: 10.1109/TPWRS.2021.3061584.

[71]  H. Bevrani, *Robust Power System Frequency Control*. Springer US, 2009.

[72]  H. Wu, K. S. Tsakalis, and G. T. Heydt, "Evaluation of time delay effects to wide area power system stabilizer design," *IEEE Trans. Power Syst.*, vol. 19, no. 4, pp. 1935–1941,

Nov. 2004, doi: 10.1109/TPWRS.2004.836272.

[73]  S. Sonmez, S. Ayasun, and C. O. Nwankpa, "An exact method for computing delay margin for stability of load frequency control systems with constant communication delays," *IEEE Trans. Power Syst.*, vol. 31, no. 1, pp. 370–377, Jan. 2016, doi: 10.1109/TPWRS.2015.2403865.

[74]  M. Liu, L. Yang, D. Gan, D. Wang, F. Gao, and Y. Chen, "The stability of AGC systems with commensurate delays," *Eur. Trans. Electr. Power*, vol. 17, no. 6, pp. 615–627, Nov. 2007, doi: 10.1002/etep.159.

[75]  V. V. Viswanathan and M. Kintner-Meyer, "Second use of transportation batteries: Maximizing the value of batteries for transportation and grid services," *IEEE Trans. Veh. Technol.*, vol. 60, no. 7, pp. 2963–2970, Sep. 2011, doi: 10.1109/TVT.2011.2160378.

[76]  "Generic Models (PV Plants) - ESIG." .

[77]  T. G. S. H. Li, J. L. Wert, A. B. Birchfield, T. J. Overbye, T. E.- Roman, C. M. Domingo, F. E. P. Marcos, P. D. Martinez, and  and B. P. Gindy, "Building Highly Detailed Synthetic Electric Grid Data Sets for Combined Transmission and Distribution Systems," *Open Acess J. Power Energy*, vol. 7, pp. 478–488, 2020.

[78]  "Fact #995, September 18, 2017: Electric Vehicle Charging at Home Typically Draws Less Than Half the Power of an Electric Furnace | Department of Energy." .